CMS Draft Analysis Note

The content of this note is intended for CMS internal use and distribution only

Searches for dijet resonances in pp collisions at $\sqrt{s} = 13$ TeV using up to 36 fb^{-1}

Magda Diamantopoulou[1], Dimitris Karasavvas[1], Niki Saoulidou[1], Eirini Tziaferi[1], Dustin Anderson[2], Maurizio Pierini[3], Serdal Damarseckin[4], Yalcin Guler[4], Javier Duarte[5], Robert Harris[5], Juska Pekkanen[6], Mikko Voutilainen[6], Giulia D'imperio[7], Federico Preiato[7], Chiara Rovelli[7], Francesco Santanastasio[7], Federico De Guio[8], Emine Gurpinar[8], Shuichi Kunori[8], Sung-Won Lee[8], (Tyler) Zhixing Wang[8], and Bora Isildak[9]

[1] National and Kapodistrian University of Athens
[2] California Institute of Technology
[3] CERN
[4] Cukurova University
[5] Fermilab
[6] University of Helsinki
[7] Sapienza, Universita di Roma and INFN
[8] Texas Tech University
[9] Middle East Technical University

Abstract

Searches for dijet resonances at $\sqrt{s} = 13$ TeV using up to 36.4 fb^{-1} from 2016 running and targeting the Moriond 2017 conference are presented.

Contents

1 Introduction

The search for resonances decaying to dijets is a long-standing effort at hadron colliders [1]. Here we report the results of the searches with data collected in 2016 at $\sqrt{s} = 13$ TeV. The analysis follows closely the searches that have been conducted eight times in the past at CMS and shown in table 1.

In this analysis note we present the analyses to be approved for release for Winter 2017 conferences. This includes a search at high mass using PF reco jets and a search at low mass using jets from calo scouting.

Year	Lumi (fb^{-1})	$\sqrt{s}$ (TeV)	EXO CADI	Pub.	Narrow Resonance	B-Tag Res.	Black Hole	Wide Res.	Dark Matt.	Scout Data
2010	0.003	7	10-010	[2]	X					
2011	1	7	11-015	[3]	X					
2012	5	7	11-094	[4]	X	X	X			
2013	4	8	12-016	[5]	X					
2014	20	8	12-059	[6]	X	X	X	X		
2015	19	8	14-005	[7]	X					X
2015	2.4	13	15-001	[8]	X					
2016	12.9	13	16-032	[9]	X				X	X

Table 1: History of Dijet Resonance Search at CMS, including the approximate year of the analysis, the luminosity, collision energy, the EXO CADI number, publication, the categories of models for which limits were published, and whether the analysis used scouting data.

1.1 Models of New Heavy Resonances

We search for processes producing narrow resonances, X, decaying to dijets as illustrated in fig. 1: $pp \rightarrow X \rightarrow jet + jet$ (inclusive).
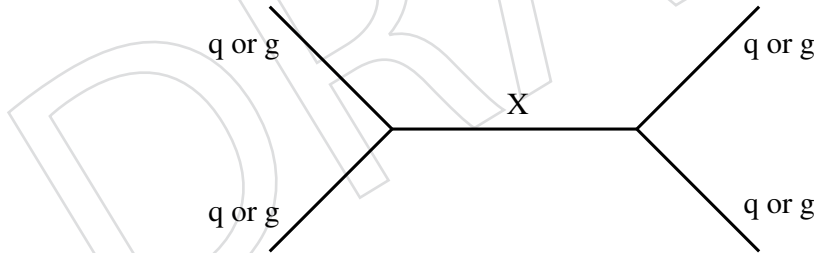
Figure 1: Feynman Diagram of dijet resonance. The initial state and final state both contain two partons (quarks, antiquarks or gluons) and the intermediate state contains an s-channel resonance X.

Here we introduce some models, say a few words about the cross section, and explicitly list the partons involved in the production, which are identical to the partons involved in the decays considered. When calculating the cross section for the models below we only consider the decays of the model to dijets, and do not consider the contribution from any decays to top quarks. Table 2 summarizes some properties of these models.

1. The model with the largest cross section is a model of string resonances. These are Regge excitations of the quarks and gluons in open string theory, which includes resonances in three parton-parton channels (predominantly qg at LHC but also some $q\bar{q}$ and gg)

with multiple spin states and quantum numbers [10, 11]. The string resonance model is discussed in detail in the appendix of Ref. [12].

2. Excited states of composite quarks [13] are strongly produced giving large cross sections (qg → q*). This is the most commonly sought benchmark model in searches for dijet resonances and the dominant decay mode is qg. We use the cannonical model in which the compositeness scale Λ is set equal to the resonance mass, all the couplings are the same as in the standard model, and we consider production of u^* and d^* and their decays decays to ug and dg.

3. Axigluons [14] or colorons [15] from an additional color interaction are also strongly produced, but require an antiquark in the initial state (q$\bar{q}$ → A or C) slightly reducing the cross section compared to excited quarks.

4. Diquarks [16] from superstring-inspired E_6 grand unified models are produced with electromagnetic coupling from the valence quarks of the proton (ud → D). The cross section for E_6 diquarks is large despite the relatively weak coupling because of the large parton distribution function for valence quarks: at high parton momentum the probability of finding a quark in the proton is significantly larger than the probability of finding a gluon or antiquark.

5. The color octet scalar resonance [17] is a generic representation for a spin-0 colored octet state in many dynamical electroweak symmetry breaking (EWSB) models such as technicolor. We consider the decay channel into a pair of gluons. The cross section is relatively large because of the strong coupling. We note that the anomalous coupling of the color-octet scalar model used is $k_s^2 = 1/2$ [18].

6. Heavy W and Z bosons [19] (called henceforth W′ and Z′) inspired by left-right symmetric grand unified models, have electroweak couplings and require antiquarks for their production($q_1\bar{q}_2$ → W′, q$\bar{q}$ → Z′), giving small cross sections. As in the standard model the Z′ production rate is expected to be smaller than W′.

7. Dark matter mediators [20, 21] following the recommendations of Ref. [20] within a simplified model [21] are assumed to be spin-1 particle and to decay only to q$\bar{q}$ and pairs of DM particles, with unknown mass m_{DM}, and with a universal quark coupling $g_q = 0.25$ and a DM coupling $g_{DM} = 1.0$. Unless otherwise noted we assume $m_{DM} = 1$ GeV, indistinguishable from zero. The cross sections for the dark matter mediator are small, comparable to the Z′ with standard model couplings.

8. Randall Sundrum gravitons [22], with coupling $k/M_{PL} = 0.1$ from the RS1 model with a warped extra dimension, are produced from gluons or quark-antiquark pairs in the initial state (q$\bar{q}$, gg → G).

1.2   Summary of Experimental Technique

Our experimental technique starts with a measurement of the inclusive process pp → jet + jet + anything. Inclusive means we measure processes containing at least two jets in the final state, but the events are allowed to contain additional jets, or anything else. The dijet system is represented by the two highest p_T jets, i.e. the two leading jets. Within the standard model our dataset is expected to be overwhelmingly dominated by the 2 → 2 process of hard parton scatters, with additional radiation off the initial and final state partons naturally giving additional jets. We do not cut away events that contain this radiation, which would reduce signals that

Model Name	X	Color	J^P	$\Gamma/(2M)$	Decay Channel
Excited Quark	q*	Triplet	$1/2^+$	0.02	qg
E_6 Diquark	D	Triplet	0^+	0.004	qq
Axigluon	A	Octet	1^+	0.04	$q\bar{q}$
Coloron	C	Octet	1^-	0.04	$q\bar{q}$
Color Octet Scalar	s_8	Octet	0^+	0.03	gg
Heavy W	W'	Singlet	1^-	0.01	$q\bar{q}$
Heavy Z	Z'	Singlet	1^-	0.01	$q\bar{q}$
Dark Matter Mediator		Singlet	$1^\pm$	0.02	$q\bar{q}$
RS Graviton	G	Singlet	2^+	0.01	$q\bar{q}, gg$

Table 2: Properties of Some Resonance Models

also have similar amounts of radiation, and unnecessarily restrict signals to a narrow topology. The events can also contain additional particles, such as leptons or photons, but this will occur very rarely in the standard model. Finally, even more rarely within the standard model, the two leading reconstructed jets in the event can result from electrons, photons or taus producing energy in the calorimeter, and we do not exclude these insignificant contributions to our sample either. We do remove however jets with large energy contribution from a reconstructed muon ($> 80\%$) in order to suppress some backgrounds produced by the presence of a mis-reconstructed high p_T muon. Our dijet selection is open to many signals of new physics including high pt jets, leptons (excluding muons) and photons. However, our selection is optimized for signals in the $2 \rightarrow 2$ parton scattering process, and is overwhelmingly dominated by the signal background of dijets from QCD within the standard model.

Our experimental method to search for dijet resonances utilizes the dijet mass spectrum measured from the two leading "wide jets" in the data. Wide jets are reconstructed by clustering jets with $\Delta R < 1.1$ from the two leading jets. This is done in order to recover the final state radiation from the two leading jets and it improves the dijet mass resolution. More details are given later. If a dijet resonance exists, it should appear in the dijet mass spectrum as a bump. First we compare the dijet mass data to QCD predictions from PYTHIA, but we do not use the MC to model our background in the search. We use a smooth function to model our standard model background as a function of dijet mass. The fit residuals shows us whether the data is smooth, which is the first test for the presence of a resonance. We look at the difference between the data and the fit, and estimate the significance when interpreted as a narrow resonance. We find no evidence for dijet resonances and we set limits on their production. The dijet resonance shape for generic di-parton resonances containing qq, qg and g g partons were simulated using PYTHIA, and used as resonance signals. To calculate the upper cross section limit for this dijet resonance shape in our data, we use the standard COMBINE statistical tool and CL_s in the frequenstist approach.

2 Data Sample

2.1 High-mass RECO analysis

We use standard MINIAOD data samples in this analysis, summarized in Table 3. Some of the data sets listed may not contain certified luminosity and thus do not contribute to the result. The total integrated luminosity calculated with normtag_DATACERT.json as of 23 Jan 2017 is 36.8 fb^{-1}.

Table 3: Data sets used in the high-mass RECO analysis.

Dateset
/JetHT/Run2016B-23Sep2016-v1/MINIAOD
/JetHT/Run2016B-23Sep2016-v3/MINIAOD
/JetHT/Run2016C-23Sep2016-v1/MINIAOD
/JetHT/Run2016D-23Sep2016-v1/MINIAOD
/JetHT/Run2016E-23Sep2016-v1/MINIAOD
/JetHT/Run2016F-23Sep2016-v1/MINIAOD
/JetHT/Run2016G-23Sep2016-v1/MINIAOD
/JetHT/Run2016H-PromptReco-v1/MINIAOD
/JetHT/Run2016H-PromptReco-v2/MINIAOD
/JetHT/Run2016H-PromptReco-v3/MINIAOD

2.2 Low-mass Calo scouting analysis

The analysis is performed on the data collected in the CMS Calo Scouting stream in 2016. This stream contains the events triggered by a dedicated set of scouting trigger paths. Events in this stream do not undergo prompt reconstruction; instead, the relevant physics objects are reconstructed at the HLT level and saved directly. For each event, the list of the calojet four momenta and some additional information (e.g., the amount of missing transverse energy in the event) is saved. The number of reconstructed vertices is also stored for events in which track reconstruction is performed by one or more other HLT paths in the menu.

We use two Calo Scouting data samples in this analysis, summarized in Table 4. The ScoutingCaloHT dataset is used to select events for the analysis signal region. It contains events selected by a trigger that requires $H_T > 250$ GeV at the HLT level. The ScoutingCaloCommissioning dataset contains events triggered by a set of looser prescaled HLT paths. This dataset is used to study the efficiency of the main H_T trigger.. In the ScoutingCaloMonitoring dataset for the event both Calo HLT jets and PF Reco jets are saved in order to perform a comparison between the fully calibrated jets and the HLT jets.

Due to the trigger inefficiency in the last data-taking period, it has been not possible to include the Run2016H in the calo scouting analysis. The total integrated luminosity calculated with normtag_DATACERT.json as of 23 Jan 2017 is 27.6 fb^{-1}.

Table 4: Data sets used in the low-mass HLT analysis.

ScoutingCaloHT samples
/ScoutingCaloHT/Run2016B-v1/RAW
/ScoutingCaloHT/Run2016B-v2/RAW
/ScoutingCaloHT/Run2016C-v2/RAW
/ScoutingCaloHT/Run2016D-v2/RAW
/ScoutingCaloHT/Run2016E-v2/RAW
/ScoutingCaloHT/Run2016F-v1/RAW
/ScoutingCaloHT/Run2016G-v1/RAW
ScoutingCaloCommissioning samples
/ScoutingCaloCommissioning/Run2016B-v1/RAW
/ScoutingCaloCommissioning/Run2016B-v2/RAW
/ScoutingCaloCommissioning/Run2016C-v2/RAW
/ScoutingCaloCommissioning/Run2016D-v2/RAW
/ScoutingCaloCommissioning/Run2016E-v2/RAW
/ScoutingCaloCommissioning/Run2016F-v1/RAW
/ScoutingCaloCommissioning/Run2016G-v1/RAW
ScoutingCaloMonitor samples
/ParkingScoutingMonitor/Run2016B-PromptReco-v1/MINIAOD
/ParkingScoutingMonitor/Run2016B-v1/RAW
/ParkingScoutingMonitor/Run2016B-PromptReco-v2/MINIAOD
/ParkingScoutingMonitor/Run2016B-v2/RAW
/ParkingScoutingMonitor/Run2016C-PromptReco-v2/MINIAOD
/ParkingScoutingMonitor/Run2016C-v2/RAW
/ParkingScoutingMonitor/Run2016D-PromptReco-v2/MINIAOD
/ParkingScoutingMonitor/Run2016D-v2/RAW
/ParkingScoutingMonitor/Run2016E-PromptReco-v2/MINIAOD
/ParkingScoutingMonitor/Run2016E-v2/RAW
/ParkingScoutingMonitor/Run2016F-PromptReco-v1/MINIAOD
/ParkingScoutingMonitor/Run2016F-v1/RAW
/ParkingScoutingMonitor/Run2016G-PromptReco-v1/MINIAOD
/ParkingScoutingMonitor/Run2016G-v1/RAW

3 Monte Carlo Samples

The analysis uses centrally produced Monte Carlo (MC) from the RunIISpring16 campaign. The GEN-SIM was produced using CMSSW_7_1_X and the DIGI-RECO was produced using CMSSW_8_0_X. Both signal and background samples were generated with PYTHIA 8 and simulated with 25 ns bunch crossings and asymptotic pileup conditions. The jets are fully constructed and are pileup mitigated with charged hadron subtraction.

3.1 Background samples

The MC samples for the QCD multijet background are binned in $\hat{p}_T$ starting at 50 GeV. The datasets are listed in Table 5.

Dataset	Cross section [pb]	Events	Equivalent luminosity [fb^{-1}]
/QCD_Pt_50to80_TuneCUETP8M1_13TeV_pythia8/RunIISpring16MiniAODv2-PUSpring16_80X_mcRun2_asymptotic_2016_miniAODv2_v0-v1/MINIAODSIM	19204300	9,968,410	5.191×10^{-4}
/QCD_Pt_80to120_TuneCUETP8M1_13TeV_pythia8/RunIISpring16MiniAODv2-PUSpring16_80X_mcRun2_asymptotic_2016_miniAODv2_v0-v1/MINIAODSIM	2762530	9,968,410	0.003608
/QCD_Pt_120to170_TuneCUETP8M1_13TeV_pythia8/RunIISpring16MiniAODv2-PUSpring16_80X_mcRun2_asymptotic_2016_miniAODv2_v0-v1/MINIAODSIM	471100	6,863,827	0.01457
/QCD_Pt_170to300_TuneCUETP8M1_13TeV_pythia8/RunIISpring16MiniAODv2-PUSpring16_80X_mcRun2_asymptotic_2016_miniAODv2_v0-v1/MINIAODSIM	117276	6,914,086	0.05896
/QCD_Pt_300to470_TuneCUETP8M1_13TeV_pythia8/RunIISpring16MiniAODv2-PUSpring16_80X_mcRun2_asymptotic_2016_miniAODv2_v0-v1/MINIAODSIM	7823	5,970,600	0.7632
/QCD_Pt_470to600_TuneCUETP8M1_13TeV_pythia8/RunIISpring16MiniAODv2-PUSpring16_80X_mcRun2_asymptotic_2016_miniAODv2_v0-v1/MINIAODSIM	648.2	3,928,870	6.061
/QCD_Pt_600to800_TuneCUETP8M1_13TeV_pythia8/RunIISpring16MiniAODv2-PUSpring16_80X_mcRun2_asymptotic_2016_miniAODv2_v0-v1/MINIAODSIM	186.9	3,959,768	21.19
/QCD_Pt_800to1000_TuneCUETP8M1_13TeV_pythia8/RunIISpring16MiniAODv2-PUSpring16_80X_mcRun2_asymptotic_2016_miniAODv2_v0-v1/MINIAODSIM	32.293	3,924,080	121.5
/QCD_Pt_1000to1400_TuneCUETP8M1_13TeV_pythia8/RunIISpring16MiniAODv2-PUSpring16_80X_mcRun2_asymptotic_2016_miniAODv2_v0-v1/MINIAODSIM	9.4183	2,999,069	318.4
/QCD_Pt_1400to1800_TuneCUETP8M1_13TeV_pythia8/RunIISpring16MiniAODv2-PUSpring16_80X_mcRun2_asymptotic_2016_miniAODv2_v0-v1/MINIAODSIM	0.84265	396,409	470.4
/QCD_Pt_1800to2400_TuneCUETP8M1_13TeV_pythia8/RunIISpring16MiniAODv2-PUSpring16_80X_mcRun2_asymptotic_2016_miniAODv2_v0-v1/MINIAODSIM	0.114943	396,100	3.446×10^3
/QCD_Pt_2400to3200_TuneCUETP8M1_13TeV_pythia8/RunIISpring16MiniAODv2-PUSpring16_80X_mcRun2_asymptotic_2016_miniAODv2_v0-v1/MINIAODSIM	0.00682981	399,226	5.845×10^4
/QCD_Pt_3200toInf_TuneCUETP8M1_13TeV_pythia8/RunIISpring16MiniAODv2-PUSpring16_80X_mcRun2_asymptotic_2016_miniAODv2_v0-v1/MINIAODSIM	0.000165445	383,926	2.321×10^6

Table 5: MC datasets for QCD background in RunIISpring16 with cross sections, number of events, and equivalent integrated luminosities.

3.2 Signal samples

The signal samples were produced with narrow resonances (i.e., the resonance width is much smaller than the experimental mass resolution). The samples cover two combinations of production and decay modes:

- $gg \rightarrow G \rightarrow gg$
- $qq \rightarrow G \rightarrow qq$

There are mass points from 500 GeV to 9 TeV for each mode. The datasets for these samples are in Table 6.

Dataset	Events
/RSGravitonToGluonGluon_kMpl01_M_500_TuneCUETP8M1_13TeV_pythia8/RunIISpring16MiniAODv2-PUSpring16_80X_mcRun2_asymptotic_2016_miniAODv2_v0-v1/MINIAODSIM	100 000
/RSGravitonToGluonGluon_kMpl01_M_750_TuneCUETP8M1_13TeV_pythia8/RunIISpring16MiniAODv2-PUSpring16_80X_mcRun2_asymptotic_2016_miniAODv2_v0-v1/MINIAODSIM	100 000
/RSGravitonToGluonGluon_kMpl01_M_1000_TuneCUETP8M1_13TeV_pythia8/RunIISpring16MiniAODv2-PUSpring16_80X_mcRun2_asymptotic_2016_miniAODv2_v0-v1/MINIAODSIM	99 674
/RSGravitonToGluonGluon_kMpl01_M_2000_TuneCUETP8M1_13TeV_pythia8/RunIISpring16MiniAODv2-PUSpring16_80X_mcRun2_asymptotic_2016_miniAODv2_v0-v1/MINIAODSIM	100 000
/RSGravitonToGluonGluon_kMpl01_M_3000_TuneCUETP8M1_13TeV_pythia8/RunIISpring16MiniAODv2-PUSpring16_80X_mcRun2_asymptotic_2016_miniAODv2_v0-v1/MINIAODSIM	99 702
/RSGravitonToGluonGluon_kMpl01_M_4000_TuneCUETP8M1_13TeV_pythia8/RunIISpring16MiniAODv2-PUSpring16_80X_mcRun2_asymptotic_2016_miniAODv2_v0-v1/MINIAODSIM	99 854
/RSGravitonToGluonGluon_kMpl01_M_5000_TuneCUETP8M1_13TeV_pythia8/RunIISpring16MiniAODv2-PUSpring16_80X_mcRun2_asymptotic_2016_miniAODv2_v0-v1/MINIAODSIM	99 929
/RSGravitonToGluonGluon_kMpl01_M_6000_TuneCUETP8M1_13TeV_pythia8/RunIISpring16MiniAODv2-PUSpring16_80X_mcRun2_asymptotic_2016_miniAODv2_v0-v1/MINIAODSIM	99 952
/RSGravitonToGluonGluon_kMpl01_M_7000_TuneCUETP8M1_13TeV_pythia8/RunIISpring16MiniAODv2-PUSpring16_80X_mcRun2_asymptotic_2016_miniAODv2_v0-v1/MINIAODSIM	100 000
/RSGravitonToGluonGluon_kMpl01_M_8000_TuneCUETP8M1_13TeV_pythia8/RunIISpring16MiniAODv2-PUSpring16_80X_mcRun2_asymptotic_2016_miniAODv2_v0-v1/MINIAODSIM	100 000
/RSGravitonToGluonGluon_kMpl01_M_9000_TuneCUETP8M1_13TeV_pythia8/RunIISpring16MiniAODv2-PUSpring16_80X_mcRun2_asymptotic_2016_miniAODv2_v0-v1/MINIAODSIM	99 853
/RSGravitonToQuarkQuark_kMpl01_M_500_TuneCUETP8M1_13TeV_pythia8/RunIISpring16MiniAODv2-PUSpring16_80X_mcRun2_asymptotic_2016_miniAODv2_v0-v1/MINIAODSIM	99 004
/RSGravitonToQuarkQuark_kMpl01_M_750_TuneCUETP8M1_13TeV_pythia8/RunIISpring16MiniAODv2-PUSpring16_80X_mcRun2_asymptotic_2016_miniAODv2_v0-v1/MINIAODSIM	99 598
/RSGravitonToQuarkQuark_kMpl01_M_1000_TuneCUETP8M1_13TeV_pythia8/RunIISpring16MiniAODv2-PUSpring16_80X_mcRun2_asymptotic_2016_miniAODv2_v0-v1/MINIAODSIM	99 106
/RSGravitonToQuarkQuark_kMpl01_M_2000_TuneCUETP8M1_13TeV_pythia8/RunIISpring16MiniAODv2-PUSpring16_80X_mcRun2_asymptotic_2016_miniAODv2_v0-v1/MINIAODSIM	
/RSGravitonToQuarkQuark_kMpl01_M_3000_TuneCUETP8M1_13TeV_pythia8/RunIISpring16MiniAODv2-PUSpring16_80X_mcRun2_asymptotic_2016_miniAODv2_v0-v1/MINIAODSIM	100 000
/RSGravitonToQuarkQuark_kMpl01_M_4000_TuneCUETP8M1_13TeV_pythia8/RunIISpring16MiniAODv2-PUSpring16_80X_mcRun2_asymptotic_2016_miniAODv2_v0-v1/MINIAODSIM	99 817
/RSGravitonToQuarkQuark_kMpl01_M_5000_TuneCUETP8M1_13TeV_pythia8/RunIISpring16MiniAODv2-PUSpring16_80X_mcRun2_asymptotic_2016_miniAODv2_v0-v1/MINIAODSIM	100 000
/RSGravitonToQuarkQuark_kMpl01_M_6000_TuneCUETP8M1_13TeV_pythia8/RunIISpring16MiniAODv2-PUSpring16_80X_mcRun2_asymptotic_2016_miniAODv2_v0-v1/MINIAODSIM	99 901
/RSGravitonToQuarkQuark_kMpl01_M_7000_TuneCUETP8M1_13TeV_pythia8/RunIISpring16MiniAODv2-PUSpring16_80X_mcRun2_asymptotic_2016_miniAODv2_v0-v1/MINIAODSIM	99 632
/RSGravitonToQuarkQuark_kMpl01_M_8000_TuneCUETP8M1_13TeV_pythia8/RunIISpring16MiniAODv2-PUSpring16_80X_mcRun2_asymptotic_2016_miniAODv2_v0-v1/MINIAODSIM	99 956
/RSGravitonToQuarkQuark_kMpl01_M_9000_TuneCUETP8M1_13TeV_pythia8/RunIISpring16MiniAODv2-PUSpring16_80X_mcRun2_asymptotic_2016_miniAODv2_v0-v1/MINIAODSIM	100 000

Table 6: MC datasets for dijet resonances in RunIISpring16 with number of events.

4 Trigger

4.1 High-mass RECO analysis

We use all jet data in the JetHT dataset for the analysis, regardless of what trigger is used to record an event. In the full 2016 dataset our main triggers PFHT800 and PFHT900 suffer from the HLT trigger inefficiencies of post-ICHEP data taking. Thus for studying the trigger efficiency of the JetHT dataset for our analysis we include all the un-prescaled triggers to the study, which are PFHT800, PFHT900, PFJet500, CaloJet500_NoJetID and AK8PFJet450. We measure trigger efficiency with respect to SingleMuon 45 trigger only, as the low-energy PFHT triggers are also affected by the efficiency problems and thus are not considered reliable.

In the 2016 ICHEP analysis the trigger was fully efficient for dijet masses above 1058 GeV. For the full 2016 analysis we observe the trigger turn-on to be significantly affected by the HLT trigger issues (see Fig. 2). The bin where the statistical uncertainty of dijet mass spectrum and trigger efficiency are of similar magnitude starts at 1246 GeV. The statistical uncertainty in the bin 1246 – 1313 GeV is 0.08% and the trigger inefficiency at the center of this bin is 0.05%.
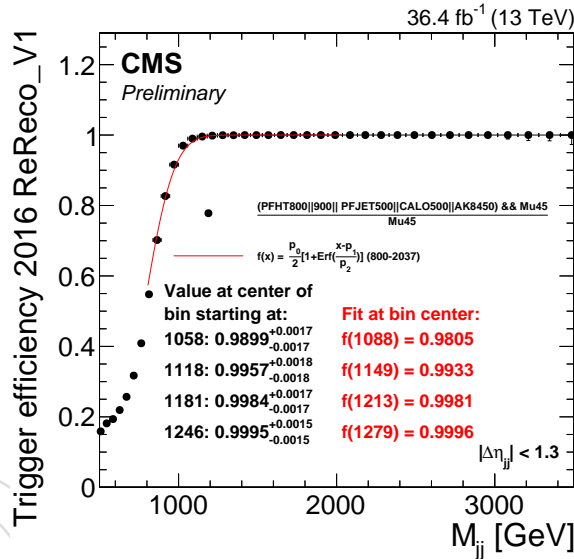

Figure 2: Efficiency of analysis triggers is measured against SingleMuon45 trigger. Turn-on is studied using all the un-prescaled triggers in the JetHT dataset, i.e. PFHT800, PFHT900, PFJet500, CaloJet500_NoJetID and AK8PFJet450. We consider triggers fully efficient starting from 1246 GeV.

4.2 Low-mass HLT analysis

The main trigger path used in this analysis is based on H_T, the scalar sum of online-reconstructed calojet p_T. The H_T-based trigger is used to inclusively select events at large transverse energy and allow a broad spectrum of analyses to be performed with the events in the scouting data streams. The trigger is seeded by L1 trigger algorithms based on H_T.

Two auxiliary scouting trigger paths are used to measure the performance of the main H_T trigger. A prescaled 'L1-only' trigger is used to measure the efficiency of the H_T trigger as a function of the dijet mass variable. This trigger imposes no cuts at HLT level, selecting all events passing the L1 H_T requirement and the trigger prescale. An even looser trigger is used to measure the efficiency of the L1 H_T seeds. This trigger is seeded by the zero-bias L1 algorithm and requires the presence of at least one calojet at HLT level.

Table 7 summarizes the details of the triggers used in the analysis. See [**?**] for a more detailed description of the scouting triggers and streams.

Table 7: Scouting trigger paths used in the analysis

Name	L1 Seeds	HLT Prescale	Selection	Purpose
HT250	HTT125 OR HTT150 OR HTT175	1	$H_T > 250\,\text{GeV}$	Main analysis trigger
L1HTT	HTT125 OR HTT150 OR HTT175	1000	None	Measure HLT efficiency
CaloJet40	ZeroBias	10	1 calojet with $p_T > 40\,\text{GeV}$	Measure L1 efficiency

Figure 3 shows the HLT trigger efficiency curve, as a function of m_{jj}. The HLT trigger efficiency is measured by using a prescaled HT trigger.

By requiring the trigger inefficiency to be comparable to the statistical error associated to the yield at a given m_{jj} value, one can derive the m_{jj} threshold from which the search should start, such that a bias caused by trigger inefficiency would be negligible. Following this procedure, we decided to run the search for events with $m_{jj} > 489\,\text{GeV}$.
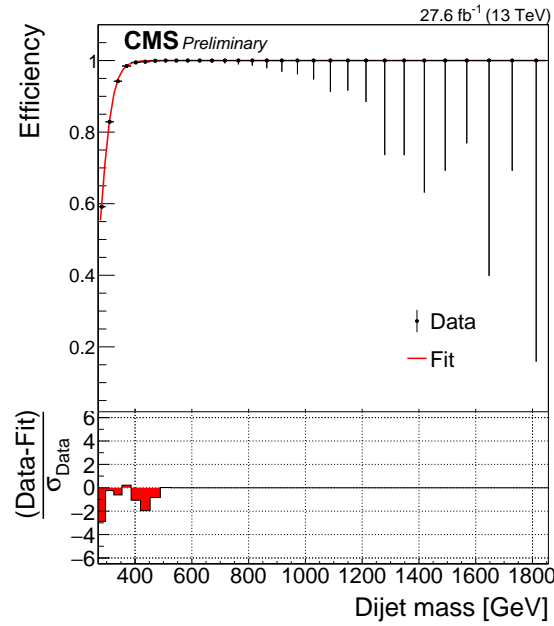

Figure 3: The measured HLT trigger efficency as a function of dijet mass for wide jets (points) compared to a parameterization from a fit to this data.

5 Event Reconstruction and Selection

The baseline event selection follows the standard of previous CMS dijet searches with small changes for the calo scouting analysis.

The jet momenta and energies are corrected using calibration constants described in Section 6. All jets are required to have $p_\mathrm{T} > 30\,\mathrm{GeV}$ and $|\eta| < 2.5$. The two jets with largest p_T are defined as the leading jets. In the standard RECO analysis we use standard PF jet ID. In the calo scouting analysis we use simple jet identification criteria by requiring that both of the leading two jets have EM and HAD fraction less 0.95.

Geometrically close jets are combined into "wide jets" and used to determine the dijet mass, as in our previous dijet searches. The wide-jet algorithm, designed for dijet resonance event reconstruction, reduces the analysis sensitivity to gluon radiation from the final state partons. The two leading jets are used as seeds and the four-vectors of all other jets, if they are within $\Delta R = \sqrt{(\Delta\eta)^2 + (\Delta\phi)^2} < 1.1$ of the seed jet, and are added to the nearest leading jet to obtain two wide jet. The above requirements maximize the search sensitivity for isotropic decays of dijet resonances in the presence of QCD dijet background.

The pseudorapidity separation of the two wide jets is required to be $|\Delta\phi_{jj}| < 1.3$. This requirement suppresses QCD t-channel, while the signal contribution significantly comes from the s-channel. It also restricts the region of our measurement predominantly within the barrel region.

Since track reconstruction is not performed for all events in Calo Scouting paths, not all of events contain a valid reconstructed interaction vertex. Therefore, no requirement on a presence of good vertex is placed in the calo scouting analysis (while it is present for the standard RECO analysis).

6 Jet Energy Corrections

6.1 High-mass RECO analysis

For the high-mass PF RECO analysis we use the most recent corrections from the JEC group, provided in the release Spring16_23Sep2016V1_DATA, consisting of L1+L2+L3 MC truth based corrections and the L2L3residual corrections derived from in-situ measurements of PF RECO data. The corrections are applied in four different intervals of validity (IOV) as recommended by the JEC group.

The JEC layers used are L1FastJet_AK4PFchs, L2Residual_AK4PFchs, L3Absolute_AK4PFchs and L2L3Residual_AK4PFchs, and the IOV versions used are BCDV1, for runs BCD, EV1 for run E, FV1 for run F early and GHV1 for runs F late, G and H. The respective run number ranges used with IOV JEC are 1 – 276823, 276824 – 277815, 277816 – 278801 and 278802 – 999999.

6.2 Low-mass Calo scouting analysis

For the low-mass Calo HLT analysis, we use a dedicated set of corrections for the first three level, L1+L2+L3, while for the L2L3Residual we use the PF Reco correction, both released by the JEC group. The JEC used are listed in table 8, in which are reported the JEC applied to the PF Reco jets saved in the monitoring datasets, and the ones applied on the HLT jets.

JEC applied on RECO jets
Spring16_25nsV10*_DATA_L1FastJet
Spring16_25nsV10*_DATA_L2Relative
Spring16_25nsV10*_DATA_L3Absolute
Spring16_25nsV10*_DATA_L2L3Residual
* = intervals of validity (IOV) as recommended by the JEC group.
JEC applied on HLT jets
80X_dataRun2_HLT_frozen_v12_L1FastJet
80X_dataRun2_HLT_frozen_v12_L2Relative
80X_dataRun2_HLT_frozen_v12_L3Absolute
Spring16_25nsV10p2_DATA_L2L3Residual

Table 8: Jet energy corrections applied on HLT jets and RECO jets

Once jets have been corrected with these corrections, a HLT-Reco comparison has been performed.

The HLT Calo jets saved in the Calo stream in general have different energy with respect to the fully reconstructed jet. A crucial aspect for this analysis is therefore to correct the HLT jet energy, or equivalently the HLT dijet invariant mass (m_{jj}), and bring it back to the true value. For this purpose the Monitoring dataset can be used where for the same events both HLT jets and RECO jets are saved.

In order to measure the jet energy scale a Tag-and-Probe method has been performed. The method consist in using the RECO jets as reference objects and compare them with the HLT jets.

The final jet energy corrections, shown in Figure 4, have been calculated using the quantity 1:

$$\frac{< p_T(HLT, probe) >}{< p_T(RECO, probe) >} \tag{1}$$

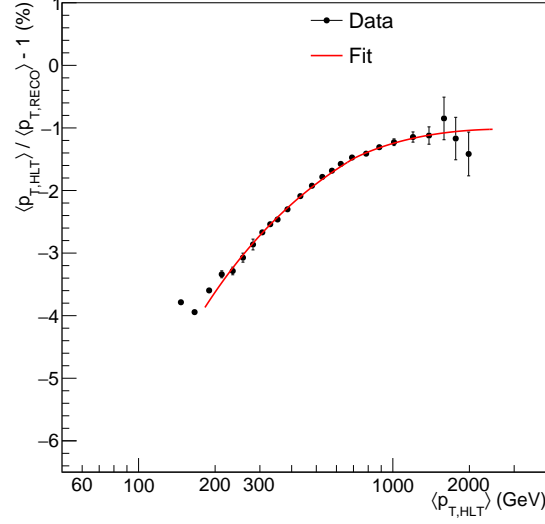248   as a function of $< p_T(HLT, probe) >$.

Figure 4: The ratio between the transverse momentum of HLT jets and the RECO jets in function of the HLT p_T.

249   The fit is performed using the equation 2.

$$fit\ function = p_0(x^{p_1}) + p_2(max(0, \log(\frac{x}{700})))^{1.2} \tag{2}$$

7 Data Quality

The main background for this analysis is the QCD multijet production. For events passing the main selection criteria, we will perform detailed data quality checks. The MC distributions shown in this section are normalized to the number of entries in the data, which is the same as multiplying the absolute PYTHIA prediction for the normalization by a factor of 0.87 (data/MC= 0.87).

Note that in addition to the main selection criteria, for these data quality plots we have also included a MET/sumET cut at 0.5, to cleanup a few jet misreconstruction problems at very high jet pt. This cut removes only 11 events with highly imbalanced dijets that are all at low dijet mass ($m_{jj} < 1.8$ TeV), and therefore do not significantly affect the dijet mass distribution itself, which has about two hundred thousand events in the mass bin at $m_{jj} = 1.8$ TeV. The jet misreconstruction problems which inspired this cleanup cut were mainly historical, and have since been mitigated with the re-reconstruction of the data (11 events removed in the re-reco sample used here, compared to 124 events in the prompt-reco sample which we no longer use).

The MET/sumET distributions and the p_T asymmetry ones after applying the MET/sumET criterion at 0.5 are shown in Fig. 5.
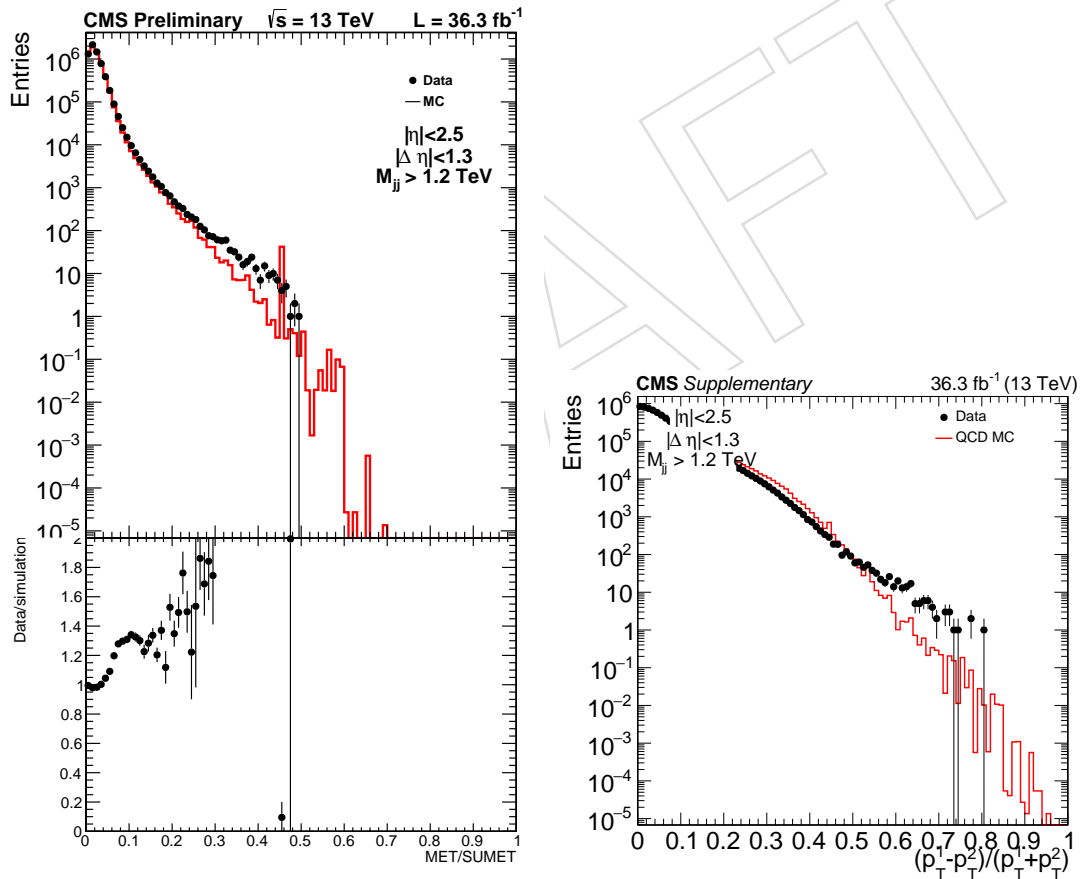

Figure 5: "PF reco data" Left: the MET/sumET distribution and Right: the p_T asymmetry distribution of events after all selection criteria are applied, for data (points) and simulated (continuous histogram) events.

Comparisons between data and simulated events: In order to examine and study the quality of our data and how robust our event and jet selection are against beam and detector related noise, detector pathologies, reconstruction catastrophic failures etc, we perform comparisons

between data and MC of basic event and jet related quantities. As far as event related distributions are concerned we examine:

- The absolute difference in pseudorapidity, $\Delta\eta = |\eta_1 - \eta_2|$, between the two leading wide-jets

- The angle between the two leading jets, $\Delta\phi = \phi_1 - \phi_2$

- The angle between the colliding partons and the scattered partons at the center-of-mass frame, $\cos(\theta^*) = \tanh([y_1 - y_2]/2)$

The second variable, $\Delta\phi = \phi_1 - \phi_2$, is also sensitive to noise and in particular noise clustered into jets. Any fake jets would distort the distribution, populated regions away from the $\Delta\phi = \pi$ expectation. The first and third variable, $\Delta\eta$ and $\cos(\theta^*)$, which shows how forward the dijet production is, is also sensitive to noise and any deviation from the expectation would be an indication of data pathologies.

Please note that the simulation used concerns Particle - Flow (PF) jets at the reconstruction level, while data utilize Calorimeter Jets at the HLT level ("CaloScouting" dataset) for the low mass analysis, and PF jets at the reconstruction level for the high mass analysis.

Stability of reconstructed quantities vs time and number of vertices: One additional important study to ensure the quality of the recorded and selected data is to examine the behavior of basic data quantities as a function of time and number of vertices (pile-up dependence). For that we examine and quantify the stability of event and jet related characteristics as a function of run number and number of reconstructed vertices for the high mass analysis.

7.1 Data vs simulation comparisons

In Figs. 6-9 we show the comparisons between data and simulated events for the variables discussed previously, for "Calo-Scouting data", and "PF-reconstructed data".

Figure 6: "Calo-Scouting data" Left: The difference in pseudorapidity between the two final wide-jets of the event, $\Delta\eta$ Right : The angle between beam axis and the dijet system at the center-of-mass frame, $\cos(\theta^*)$ of the event, after all selection criteria are applied, for data (points) and simulated (continuous histogram) events, along with their ratios (bottom plots)

Figure 7: "Calo-Scouting data" Left: The angle between the two final wide-jets of the event, $\Delta\phi$. Right : The dijet mass of the two final wide-jets of the event, after all selection criteria are applied, for data (points) and simulated (continuous histogram) events, along with their ratios (bottom plots)

We also examine the agreement between data and simulated events for the jet kinematic quantities p_T, η and ϕ, along with PF energy fractions, as well as the fraction of calorimeter jet energy in the electromagnetic and hadronic compartments of the calorimeter, as shown in Figs. 10-13 after all selection criteria are applied.

The η distribution of the data for calo jets in calo scouting in Fig. 10 is more central than the MC because the jet energy scale has an eta dependence in the data that is different than the MC. The jet energy scale has been checked to be the same in data and MC as a function of p_T and therefore also as a function of dijet mass, after all corrections, for our region of η and $\Delta\eta$. The residual difference in the η distribution between data and MC then only affects the resolution, probably marginally, and we measure the dijet mass resolution of calo jets in the data and correct the signal shapes for the difference.
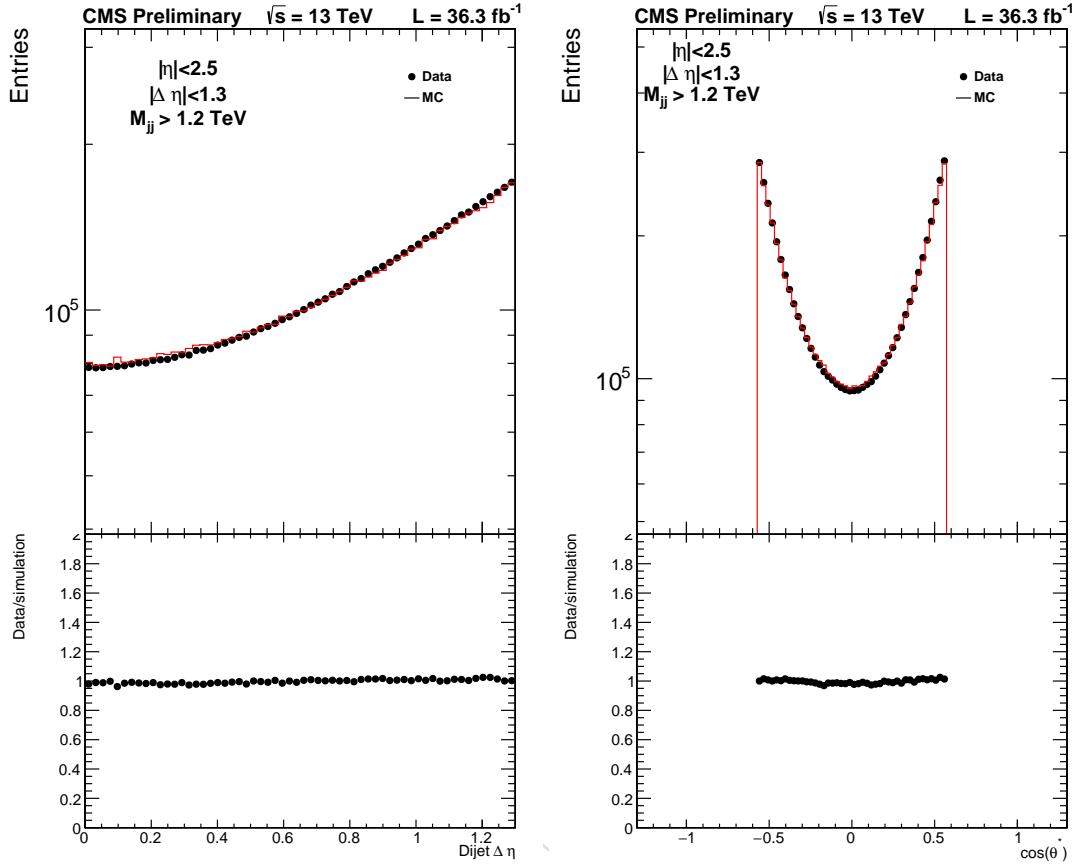
Figure 8: "PF reconstructed data" Left: The difference in pseudorapidity between the two final wide-jets of the event, $\Delta\eta$ Right : The angle between beam axis and the dijet system at the center-of-mass frame, $\cos(\theta^*)$ of the event, after all selection criteria are applied, for data (points) and simulated (continuous histogram) events, along with their ratios (bottom plots)

in Fig. 11 the fraction of jet energy in the electromagnetic calorimeter, and the fraction in the hadronic calorimeter, both show sharp edges where the distributons are cuttoff at the values 0.05 and 0.95. This is caused by the Jet ID cuts at these values of energy fraction. These distributions demonstrate that very few true jets are lost due to this Jet ID cut, which is intended to remove large noise deposits faking a high pt jet in the HCAL or ECAL. The efficiency of this cut for true dijets has been estimated from this plot and is greater than 99%.

From the jet and event related distributions it is evident that the signal sample is clean, with no pathologies and no indication of noise present, after event and jet selection criteria are applied.

7.1.1 Stability of reconstructed quantities vs time

In Figs. 14-15 we examine the stability of the dijet mass, $\cos(\theta^*) = \tanh([y_1 - y_2]/2)$ and $\Delta\phi = \phi_1 - \phi_2$ as a function of time. Event related quantities are stable as a function of time, as indicated by the absence of any significant slope in the distributions.

The jet energy fractions and the jet kinematic distributions as a function of time are shown in Figs. 16-19. There are variations present of the order of $\pm 2\%$ for the "Calo scouting" data, and $\pm 10\%$ for the "PF reconstructed" data in the jet energy fractions which do not affect the stability of the jet p_T estimation. It is evident that these variations are a result of the track recontruction problem that was mitigated online in the last part of the data-taking, where the energy fractions
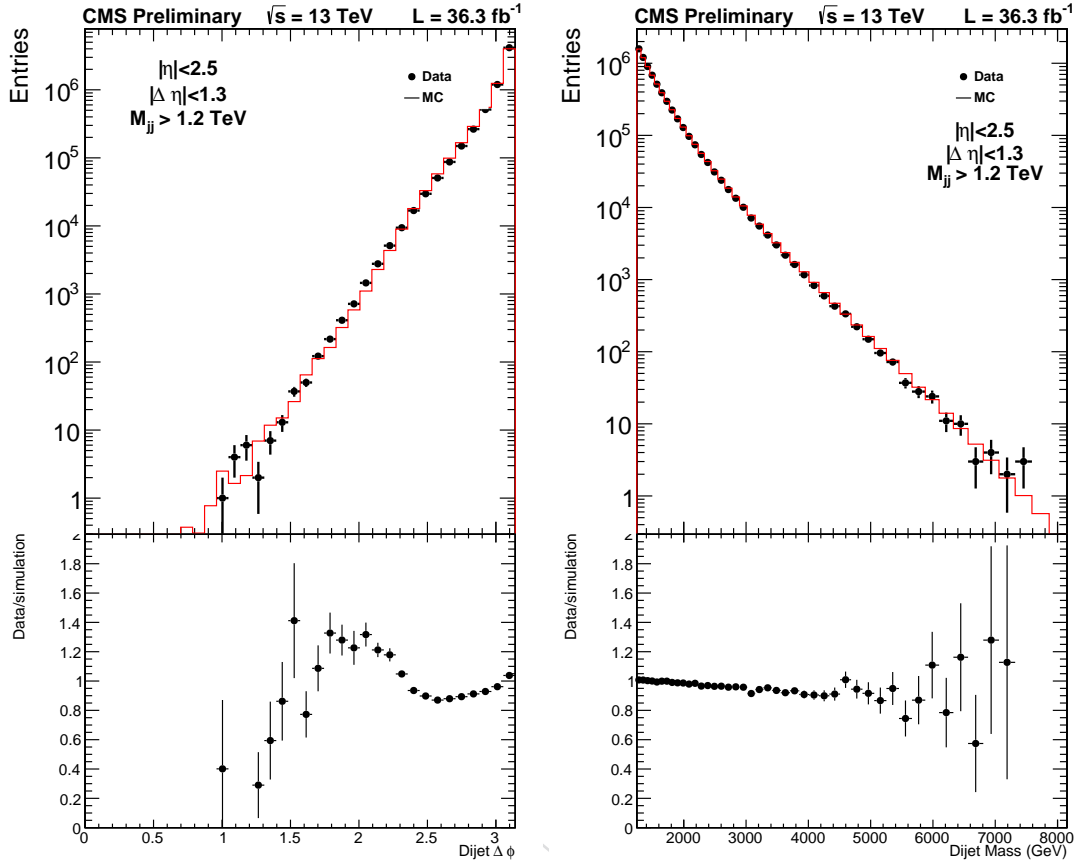
Figure 9: "PF reconstructed data" Left: The angle between the two final wide-jets of the event, $\Delta\phi$. Right : The dijet mass of the two final wide-jets of the event, after all selection criteria are applied, for data (points) and simulated (continuous histogram) events, along with their ratios (bottom plots)

Figure 10: "Calo-Scouting data": The p_T(left), η (middle), and ϕ (right) of the two leading jets wide-jets after all selection criteria are applied, for data (points) and simulated (continuous histogram) events, along with their ratios (bottom plots).

appear to be very stable.

Again the absence of any significant slope indicates that jet-related quantities are stable as a function of time.

7.1.2 Stability of reconstructed quantities vs number of vertices

In Fig. 20 we examine the stability of the dijet mass, $\cos(\theta^*) = \tanh([y_1 - y_2]/2)$ and $\Delta\phi = \phi_1 - \phi_2$ as a function of number of vertices. Event related quantities are not sensitive to pileup effects, as indicated by the absence of any significant slope in the distributions.

The jet energy fractions and the jet kinematic distributions as a function of number of vertices are shown in Figs. 21-7.1.2. There are variations present of the order of $\pm 10 - 20\%$ in the jet energy fractions which do not affect the stability of the jet p_T estimation.

Figure 11: "Calo-Scouting data": The faction of energy in the electromagnetic calorimeter for calo jets (top) for events with dijet mass above 453 GeV (left), 1 TeV (middle) and 4 TeV (right) after all selection criteria are applied. The faction of energy in the hadronic calorimeter for calo jets (bottom) for events with dijet mass above 453 GeV (left), 1 TeV (middle) and 4 TeV (right) of dijet mass after all selection criteria are applied.
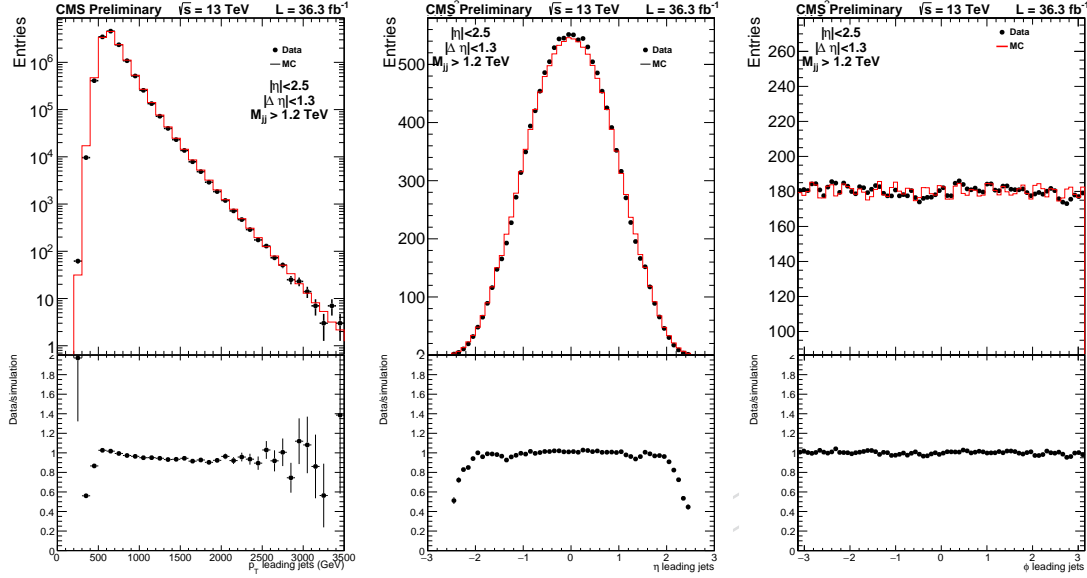
Figure 12: "PF reconstructed data": The p_T (left), η (middle), and ϕ (right) of the two leading wide-jets after all selection criteria are applied, for data (points) and simulated (continuous histogram) events, along with their ratios (bottom plots).

7.1.3 Cross section stability

Figures 23-24 show the stability of the dijet cross section (after all analysis selections) as a function of time : the cross section shows $\sim$ 10% variations in the last part of the running period, probably related with the different running conditions and hence jet energy corrections applied.

Figure 13: "PF reconstructed data": The charged hadron (left), neutral hadron (middle), and neutral EM (right) PF jet energy fractions of the two leading jets after all selection criteria are applied, for data (points) and simulated (continuous histogram) events, along with their ratios (bottom plots).

Figure 14: "Calo-Scouting data" :The dijet mass (left), $\cos(\theta^*)$ (middle) and $\Delta\phi$ (right) distributions after all selection criteria are applied as a function of time.

Figure 15: "PF reconstructed data" :The dijet mass (left), $\cos(\theta^*)$ (middle) and $\Delta\phi$ (right) distributions after all selection criteria are applied as a function of time.

Figure 16: "Calo-Scouting data" : The jet neutral hadron (left), and neutral EM (right) energy fractions after all selection criteria are applied as a function of time.

Figure 17: "Calo-Scouting data": The jet p_T (right), η (middle), and ϕ (right) energy fractions after all selection criteria are applied as a function of time.

Figure 18: "PF Reconstructed data" : The jet charged hadron (left), neutral hadron (middle), and neutral EM (right) energy fractions after all selection criteria are applied as a function of time.
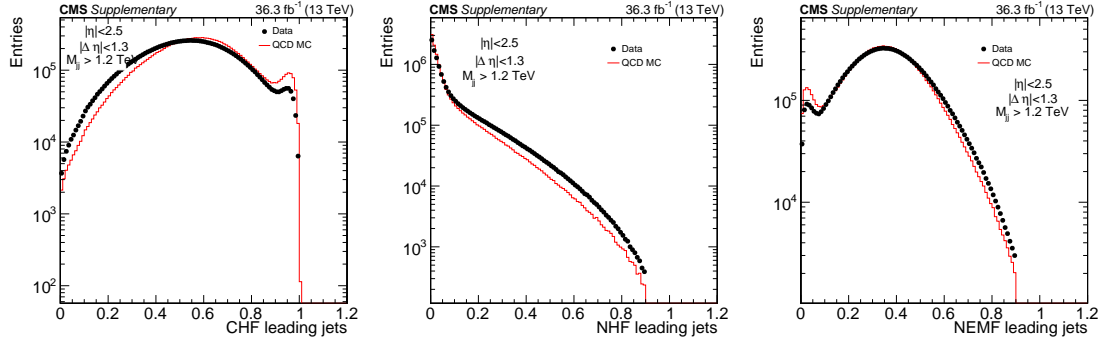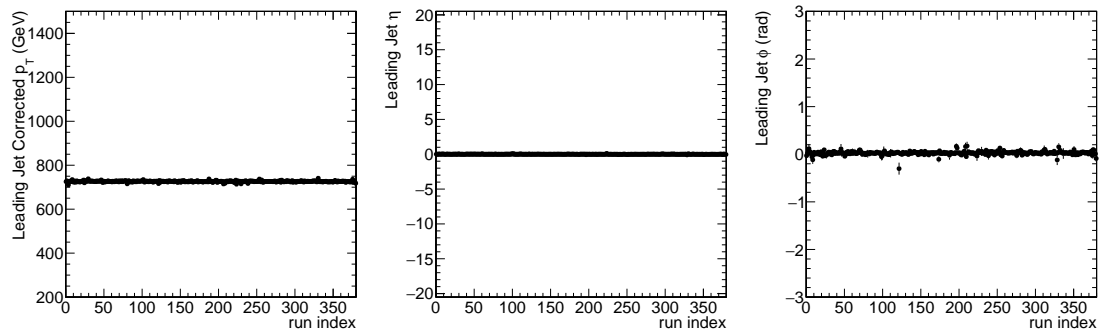

Figure 19: "PF Reconstructed data": The jet p_T (right), η (middle), and ϕ (right) after all selection criteria are applied as a function of time.
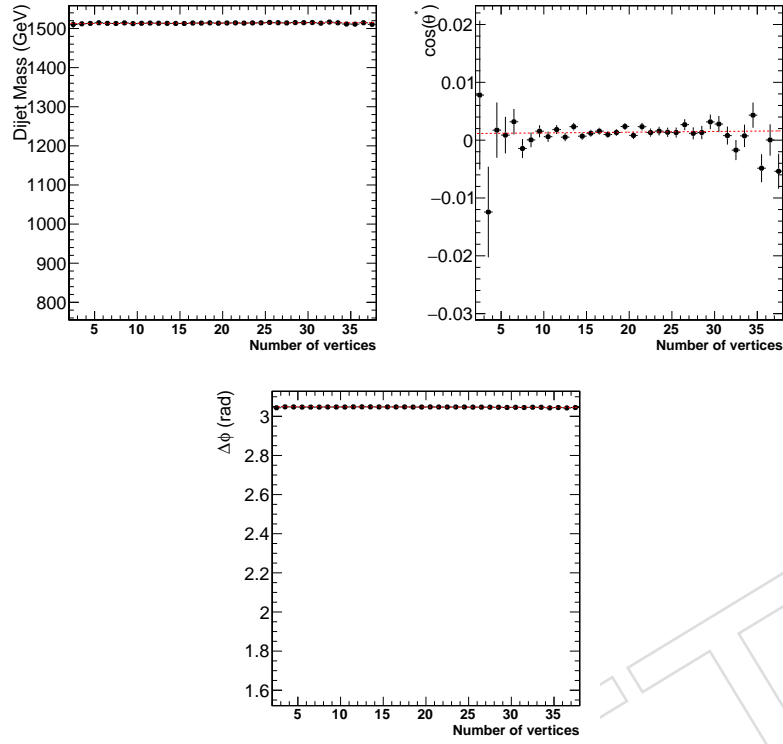
Figure 20: "PF reconstructed data" :The dijet mass (left), $\cos(\theta^*)$ (middle) and $\Delta\phi$ (right) distributions after all selection criteria are applied as a function of number of vertices.
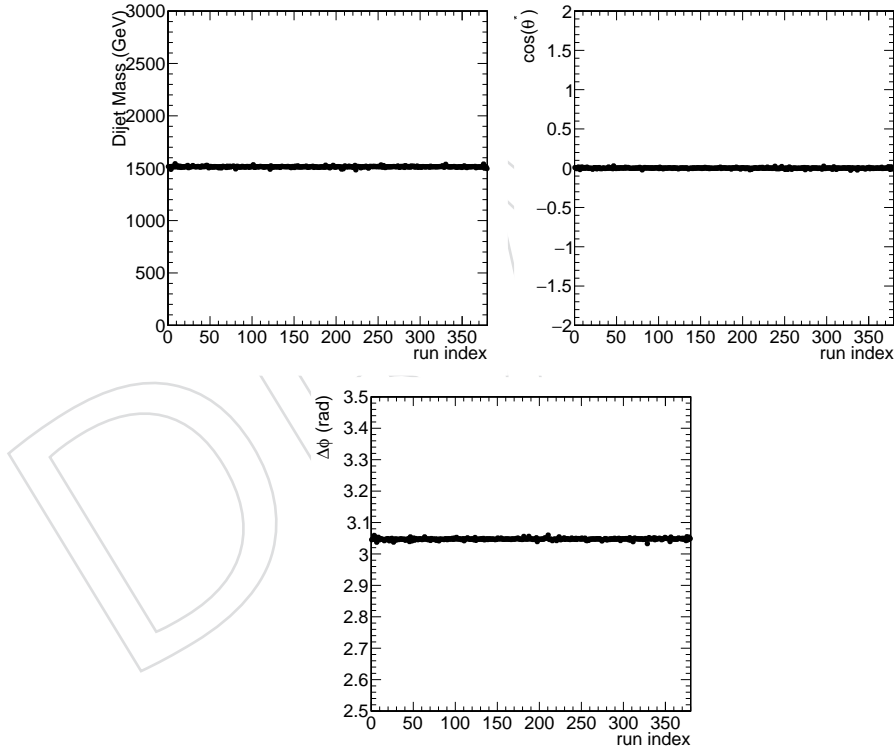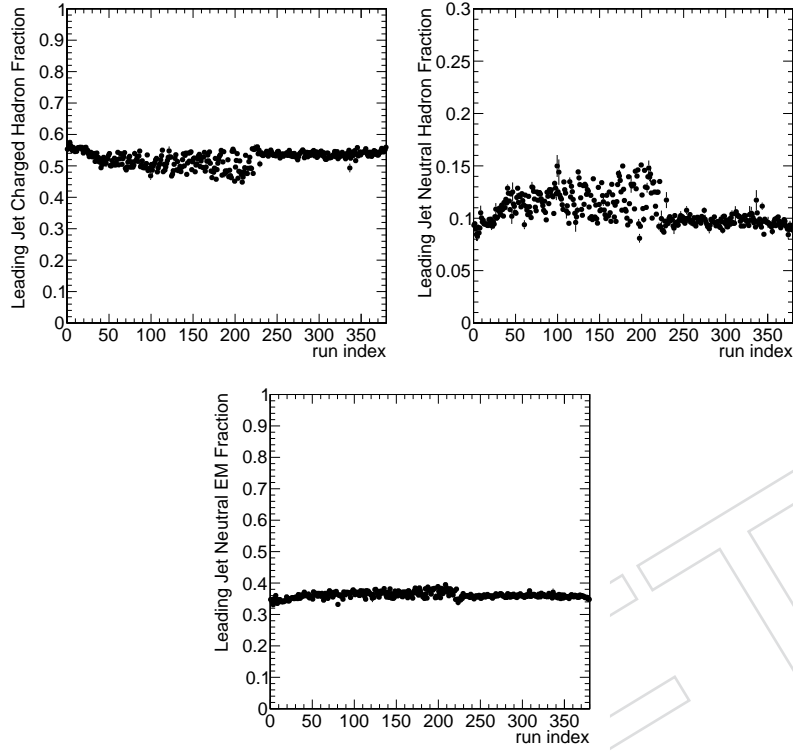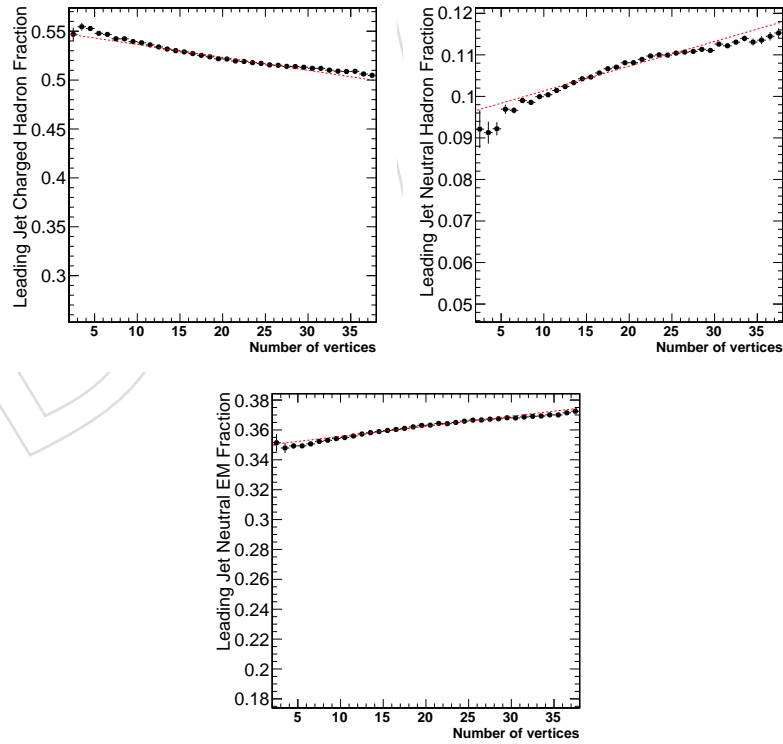

Figure 21: "PF reconstructed data" : The jet charged hadron (left) neutral hadron (middle), and neutral EM (right) energy fractions after all selection criteria are applied as a function of number of vertices.
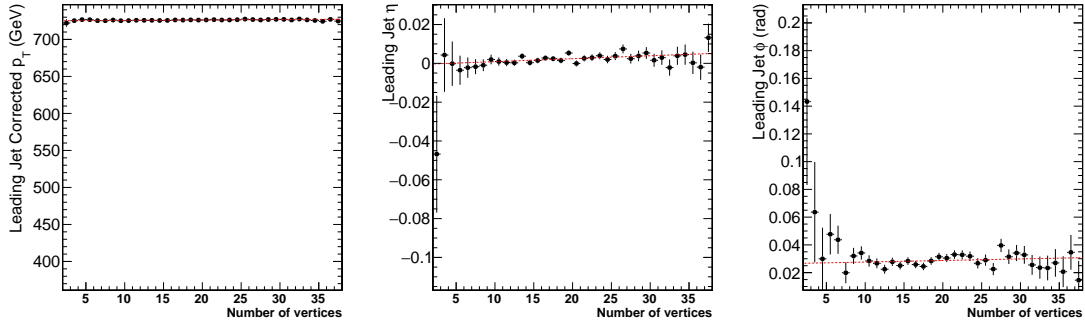
Figure 22: "PF reconstructed data": The jet p_T (right), η (middle), and ϕ (right) after all selection criteria are applied as a function of number of vertices.

Figure 23: "Calo-Scouting data" : Stability of the dijet cross section as a function of time, and after all selection criteria are applied.

Figure 24: "PF Reconstructed data" : Stability of the dijet cross section as a function of time, and after all selection criteria are applied.

8   Dijet mass spectrum and background fit

8.1   Fit method

In order to test the smoothness, we fit the dijet mass spectrum separately for the low-mass and high-mass search with a background-only function. The fit function for the high-mass analysis, defined as

$$\frac{\mathrm{d}\sigma}{\mathrm{d}m_{jj}} = \frac{p_0(1 - m_{jj}/\sqrt{s})^{p_1}}{(m_{jj}/\sqrt{s})^{p_2 + p_3 \log(m_{jj}/\sqrt{s})}} \, , \tag{3}$$

is a four-parameter continuous function that has been used extensively in previous searches to fit the falling dijet spectrum [23, 24].
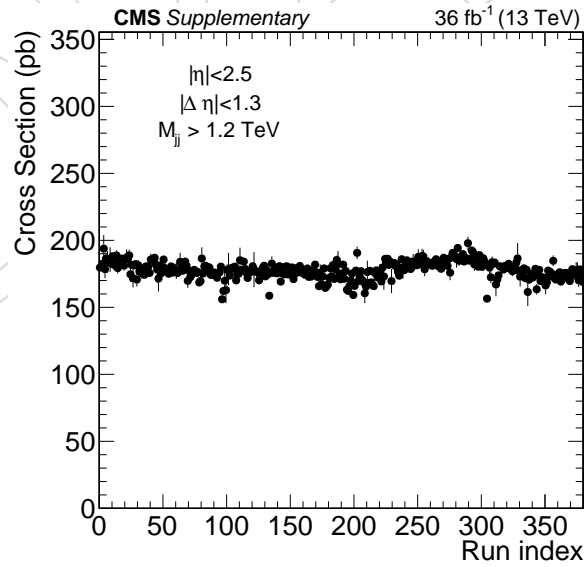
The fit function for the low-mass analysis instead is a five-parameter continuous function, defined as

$$\frac{\mathrm{d}\sigma}{\mathrm{d}m_{jj}} = \frac{p_0(1 - m_{jj}/\sqrt{s})^{p_1}}{(m_{jj}/\sqrt{s})^{p_2 + p_3 \log(m_{jj}/\sqrt{s}) + p_4 \log^2(m_{jj}/\sqrt{s})}} \, , \tag{4}$$

We perform an extended, background-only, binned, maximum likelihood fit to the 2016 data with the following likelihood,

$$\mathcal{L}(\text{data}|\boldsymbol{\theta}) = \prod_{i=1}^{n_b} \text{Poisson}(x_i | b_i(\boldsymbol{\theta})) = \prod_{i=1}^{n_b} \frac{b_i(\boldsymbol{\theta})^{x_i} e^{-b_i(\boldsymbol{\theta})}}{x_i!} \, , \tag{5}$$

where n_b is the number of bins, $\boldsymbol{\theta}$ is the vector of nuisance parameters (p_0, p_1, p_2, p_3) and p_4 for the low-mass analysis (or equivalently $(N_b, p_1, p_2, p_3, p_4)$), x_i is the data yield in bin i, and b_i is the integral of the fit function in bin i multiplied by the total number of expected events N_b,

$$b_i(\boldsymbol{\theta}) = N_b \int_{m_{jj}^{\min,i}}^{m_{jj}^{\max,i}} \mathrm{d}m_{jj} \, p(m_{jj}) \, , \tag{6}$$

where $p(m_{jj})$ is the fit function in equations 3 and 4 normalized to unity.

To test the goodness-of-fit (GOF), we define two test statistics. One is a modified chi-square,

$$\chi^2 = \sum_{i=1}^{n_b} \left(\frac{x_i - b_i}{\sigma_{x_i}} \right)^2 \, , \tag{7}$$

where we define the "uncertainty" σ_{x_i} in terms of the 68% CL region of a Poisson distribution. Technically, the defintion is as follows, setting $\alpha = 1 - 0.687$,

$$\sigma_{x_i} = \begin{cases} D_c^{-1}(\alpha/2, x_i + 1) \, , & \text{if } b_i > x_i \\ D^{-1}(\alpha/2, x_i) \, , & \text{if } b_i < x_i \end{cases} \tag{8}$$

where $D^{-1}(\alpha/2, x_i)$ is the quantile function of the gamma distribution, which is the inverse of the cumulative distribution function (lower tail) of the gamma distribution,

$$D(\alpha/2, x_i) = \int_{-\infty}^{\alpha/2} \frac{1}{\Gamma(x_i)} z^{x_i - 1} e^{-z} \, \mathrm{d}z \, , \tag{9}$$

and $D_c^{-1}(\alpha/2, x_i + 1)$ is the inverse of the cumulative distribution function (upper tail) of the gamma distribution,

$$D_c(\alpha/2, x_i + 1) = \int_{\alpha/2}^{+\infty} \frac{1}{\Gamma(x_i + 1)} z^{x_i} e^{-z} \, \mathrm{d}z \, . \tag{10}$$

Similarly, an alternative test statistic, which is a likelihood ratio with respect to the *saturated model* can also be defined,

$$-2\log\lambda(\boldsymbol{\theta}) = -2\log\frac{\prod_{i=1}^{n_b}\text{Poisson}(x_i|b_i(\boldsymbol{\theta}))}{\prod_{i=1}^{n_b}\text{Poisson}(x_i|x_i)} = 2\sum_{i=1}^{n_b}\left[b_i(\boldsymbol{\theta}) - x_i + x_i\log\frac{x_i}{b_i(\boldsymbol{\theta})}\right] . \quad (11)$$

In both cases, we generate 10,000 pseudodatasets from the best-fit model parameters on data, refit each pseudodataset with a maximum likelihood fit, and save the test statistic value.

8.2 Fit Results

The result of the background-only fit to the data is shown in Fig. 25.

Figure 25: The binned fit for PF RECO performed in the range $1246 < m_{jj} < 8152\,\text{GeV}$. The signal shapes shown are normalized to the excluded cross section for each resonance type at that mass.

In figure 26, we show the distribution of both test statistics from these pseudoexperiments as well the value observed in data. For the first test, the observed value has a p-value around 38% and the effective number of degrees of freedom (from fitting a chi-square distribution) is 37.1 ± 0.1, while for the second test the p-value is around 43% and the effective number of degrees of freedon is 42.4 ± 0.1.

The result of the background-only fit to the data for the low-mass analysis is shown in Figure 27.

In figure 28, we show the distribution of both test statistics from these pseudoexperiments as well the value observed in data. In both cases, the observed value has a p-value around 61% and the effective number of degrees of freedom is 22.8 ± 0.1.

Figure 26: Toy distribution for the goodness-of-fit study using the χ^2 test statistic (left) and the $-2 \log \lambda$ test statistic (right) as defined in the text.
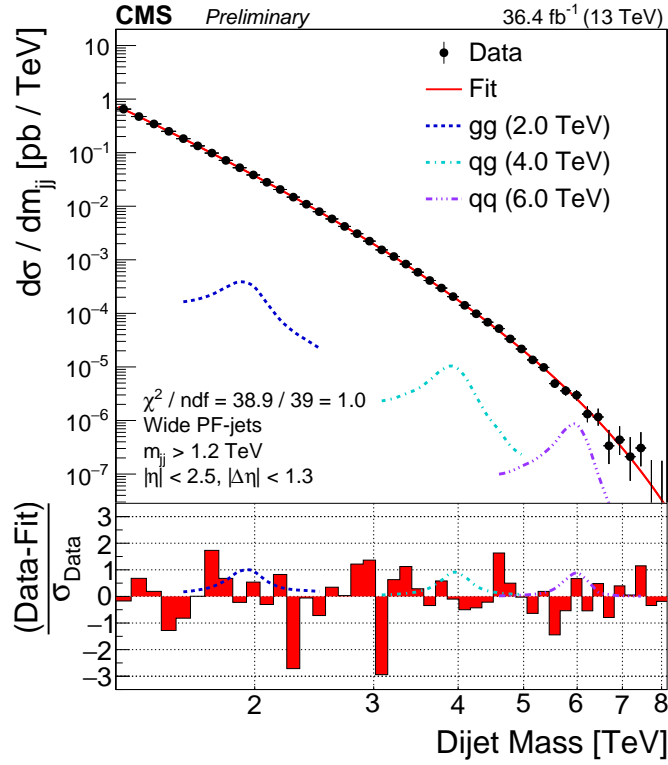

Figure 27: The binned fit for Calo HLT performed in the range $489 < m_{jj} < 2037\,\text{GeV}$. The signal shapes shown are normalized to the excluded cross section for each resonance type at that mass.
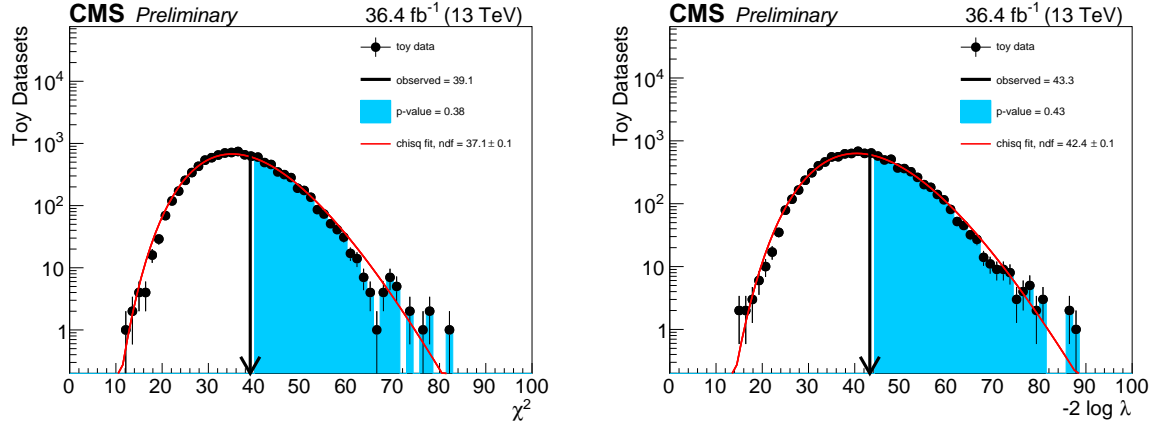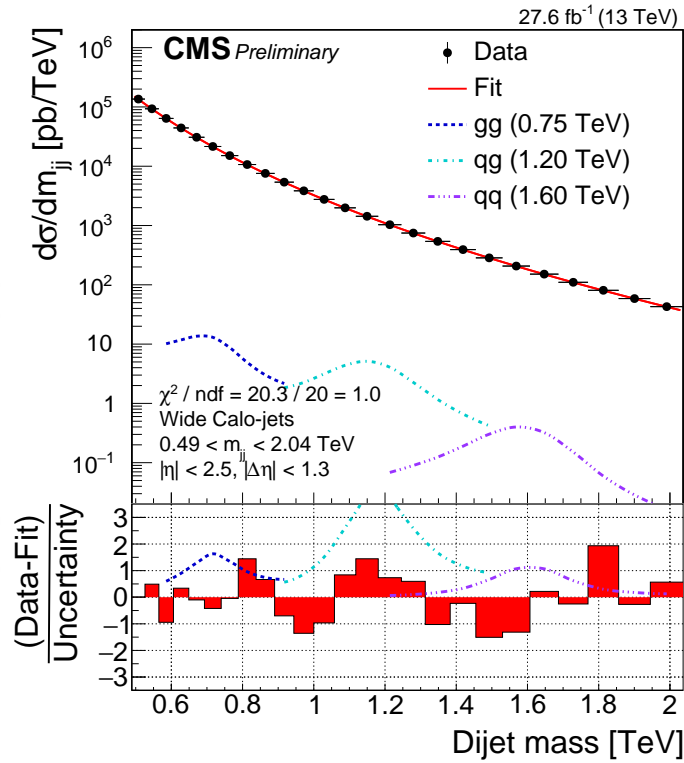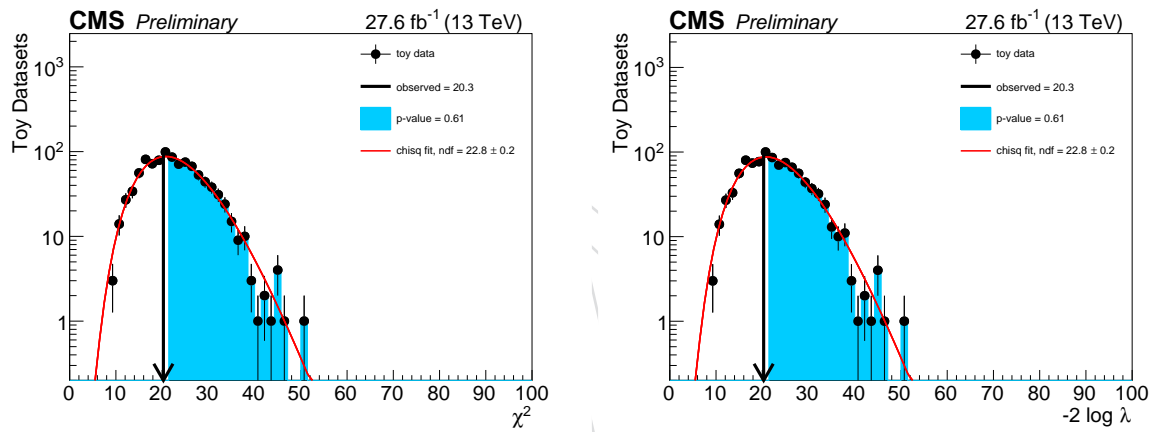
Figure 28: Toy distribution for the goodness-of-fit study using the χ^2 test statistic (left) and the $-2\log\lambda$ test statistic (right) as defined in the text.

9   Signal Shapes

9.1   High-mass RECO analysis

The signal resonance shape depends on the decay mode (gg, qg, qq, or Gaussian lineshape). Because we only consider narrow resonances, where the natural resonance width is neglibible compared to the dijet mass resolution at CMS, the natural width does not affect the resonance shape. The generic shapes for the two types of decay modes were produced from samples of the processes $gg \to G \to gg$, $qg \to q^* \to qg$, and $qq \to G \to qq$ for 11 mass points: 500 GeV, 750 GeV, and 1 TeV to 9 TeV in 1 TeV spacing. See Section 3.2 for more detail on the samples. Some of the resonance shapes are shown in Fig. 29.

To produce signal shapes at masses between the 11 generated samples, the shapes are interpolated. The method used to interpolate the shapes is the same as has been used previously in the high-mass analysis. It is described in [25].

The shapes of resonances with gg, qg, and qq final states differ due to the differences between quarks and gluons. Gluons emit more radiation than quarks, which casuses the resonance width to increase with the number of gluons in the final state. The low-mass tail of the resonance shape is due to the effect of final state radiation and the parton distribution function having higher parton luminosity at low mass than at high mass. The high-mass tail is smaller and is caused by initial state radiation. These resonance shapes are approximately valid for any model of resonances involving the same pairs of partons, assuming the relative half-width of the model $((\Gamma/2)/M)$ is small compared to the dijet mass resolution.
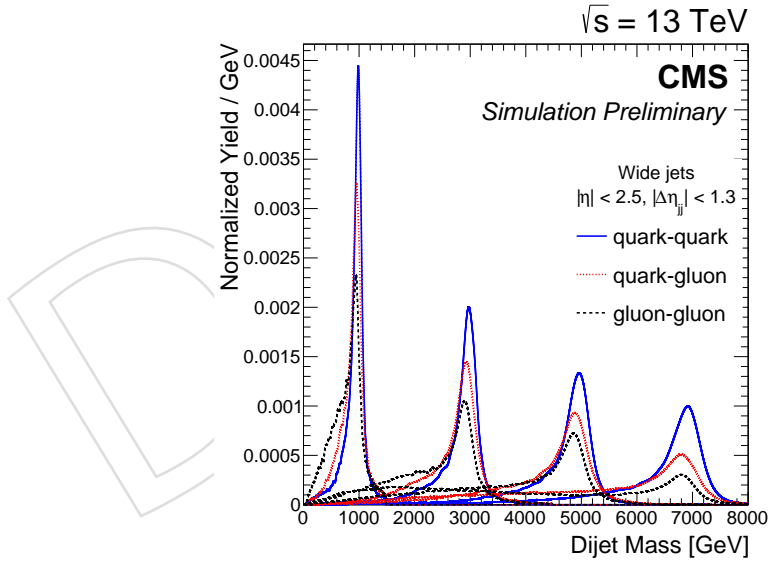
Figure 29: Signal shapes for $gg \to G \to gg$, $qg \to q^* \to qg$, and $qq \to G \to qq$ resonances. The integral of the shapes has been normalized to unity.

9.2   Low-mass calo scouting analysis

The signal resonance shapes for the calo scouting analysis are shown in Fig. 30. They are obtained by smearing the shape from the high-mass RECO analysis by a Gaussian resolution correction factor. The factor is equal to the difference in quadrature between the measured jet energy resolution for calo scouting and PF reco. This procedure is discussed further in

377 reference [26] where more details on the dijet mass resolution for calo scouting may also be
378 found.
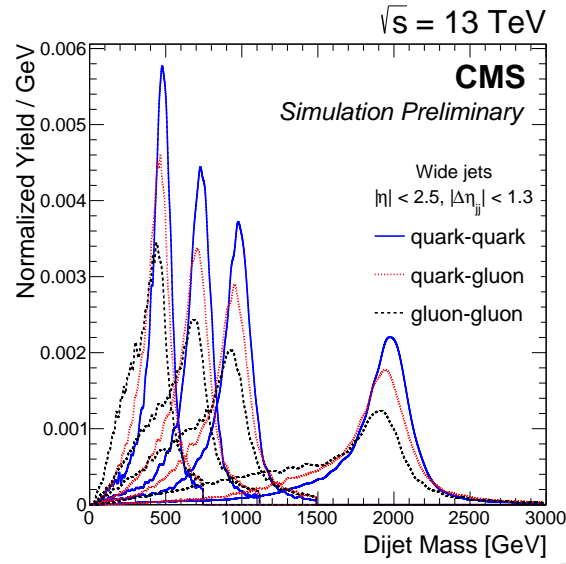
Figure 30: Signal shapes for $gg \rightarrow G \rightarrow gg$, $qg \rightarrow q^* \rightarrow qg$, and $qq \rightarrow G \rightarrow qq$ resonances. The integral of the shapes has been normalized to unity.

10   Systematic uncertainties

The systematic uncertainties propagated to the signal prediction are shown in table 9.

Table 9: Summary of systematic uncertainties propagated to the signal prediction in PF RECO analysis.

Systematic Uncertainty Source	Nominal Value	Uncertainty
Jet Energy Resolution	no smearing	10% of RECO resolution
Jet Energy Scale	no shift	$\pm 2\%$ shift of m_{jj}
Luminosity	$36.4\,\mathrm{fb}^{-1}$	$\pm 6.2\%$

11 Narrow Resonance Limits

Figure 31 shows the 95% CL asymptotic LHC CL_s limits on $\sigma \times BR \times A$ for a gg resonance, a qg resonance, and a qq resonance. Bottom right figure shows also the gg and qq resonance limits weighted for the branching ratios of a Randall-Sundrum Graviton (see Appendix C), in order to compare directly with this model cross section.

Figure 32 and Table 10 summarize the same information.
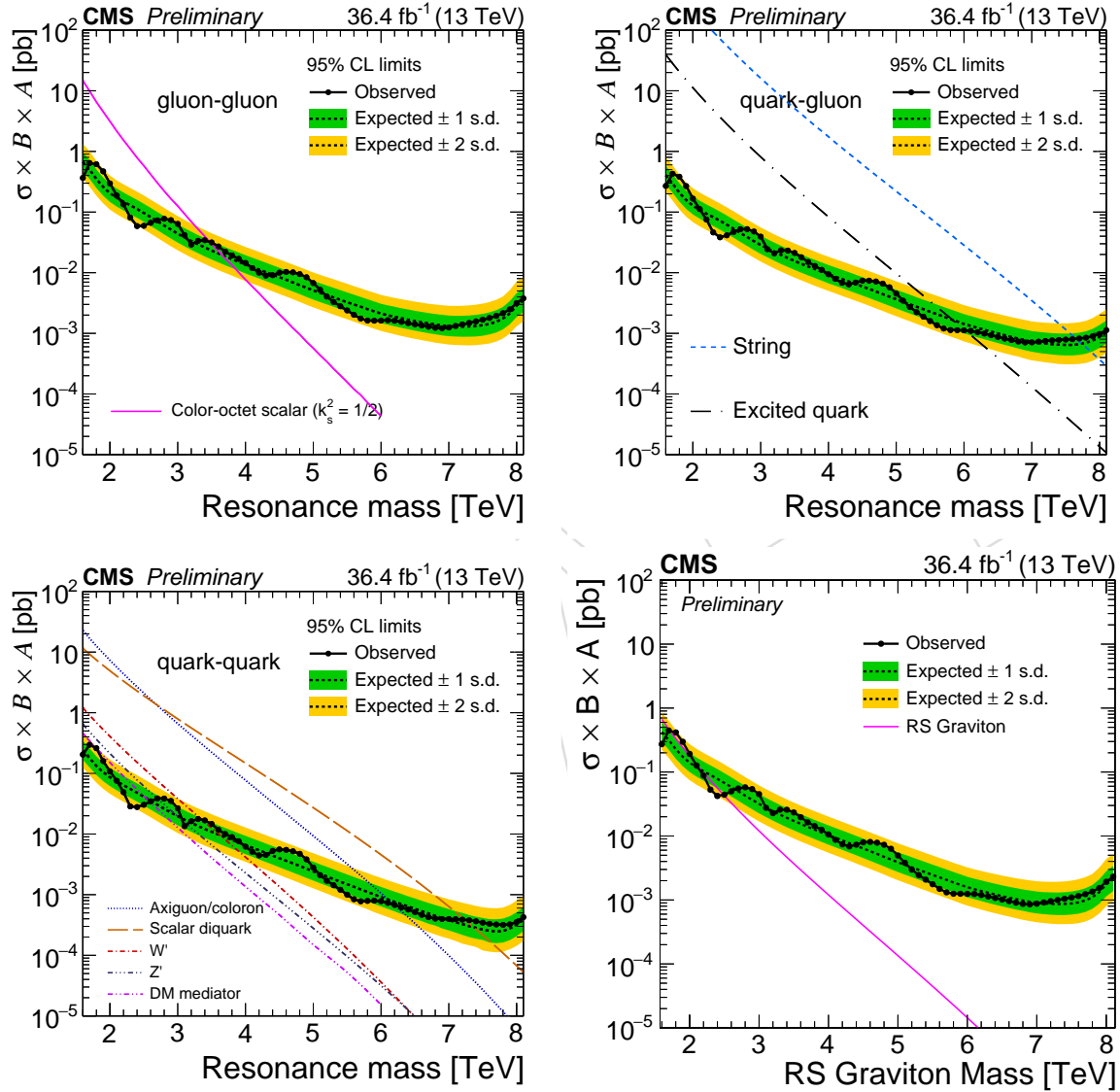
Figure 31: 95% CL asymptotic LHC CL_s limits on $\sigma \times BR \times A$ for a gg resonance (top left), a qg resonance (top right), and a qq resonance (bottom left). Bottom right plot shows the gg and qq resonance limits weighted for the branching ratios of a Randall-Sundrum Graviton.

Figure 33 shows the local significance as a function of mass for a gg resonance, a qg resonance, and a qq resonance.

Figure 34 shows the 95% CL asymptotic LHC CL_s limits on $\sigma \times BR \times A$ for a gg resonance, a qg resonance, and a qq resonance for the low-mass analysis.

Figure 35 and Table 11 summarize the same information.

Table 10: Observed and expected upper limits at 95% CL on $\sigma \times B \times A$ for a gg resonance, a qg resonance, and a qq resonance as a function of the resonance mass.

| Mass [TeV]	95% CL upper limit [pb]							
	gg		qg		qq		qq-gg for RSG	
	Observed	Expected	Observed	Expected	Observed	Expected	Observed	Expected
1.6	0.366	0.672	0.27	0.405	0.204	0.237	0.273	0.421
1.7	0.643	0.498	0.429	0.295	0.297	0.177	0.446	0.315
1.8	0.615	0.352	0.383	0.209	0.26	0.132	0.415	0.228
1.9	0.469	0.26	0.268	0.159	0.16	0.105	0.297	0.174
2.0	0.296	0.205	0.167	0.128	0.107	0.0863	0.192	0.14
2.1	0.187	0.173	0.112	0.109	0.0755	0.0736	0.126	0.119
2.2	0.134	0.148	0.0751	0.0941	0.0488	0.0639	0.088	0.103
2.3	0.0813	0.129	0.0461	0.0824	0.0285	0.0553	0.0531	0.0898
2.4	0.0587	0.112	0.0383	0.0717	0.0279	0.0479	0.0424	0.0782
2.5	0.0594	0.0965	0.0413	0.0619	0.0303	0.0412	0.0442	0.0676
2.6	0.0665	0.0828	0.047	0.0529	0.0346	0.0354	0.05	0.0583
2.7	0.073	0.0705	0.0521	0.0451	0.0387	0.0304	0.0554	0.0499
2.8	0.0776	0.06	0.0524	0.0388	0.0385	0.0261	0.0577	0.0427
2.9	0.0735	0.0514	0.0478	0.0331	0.0351	0.0226	0.0541	0.0368
3.0	0.0638	0.0439	0.0393	0.0286	0.0266	0.0196	0.0451	0.0318
3.1	0.0417	0.0382	0.0244	0.0251	0.0134	0.0172	0.0276	0.0278
3.2	0.0291	0.0333	0.0209	0.0222	0.0163	0.0153	0.0228	0.0244
3.3	0.0336	0.0294	0.0234	0.0196	0.0177	0.0135	0.0258	0.0216
3.4	0.0343	0.0261	0.0232	0.0174	0.0168	0.0121	0.0257	0.0192
3.5	0.0316	0.0231	0.0211	0.0156	0.0146	0.0109	0.0234	0.0172
3.6	0.0271	0.0208	0.018	0.014	0.0117	0.00981	0.0197	0.0155
3.7	0.0222	0.0186	0.015	0.0126	0.01	0.00881	0.0164	0.0139
3.8	0.0193	0.0167	0.0129	0.0115	0.0089	0.00798	0.0143	0.0126
3.9	0.0169	0.0151	0.0112	0.0104	0.00761	0.0072	0.0125	0.0113
4.0	0.0145	0.0136	0.00941	0.0094	0.00619	0.00652	0.0106	0.0103
4.1	0.0119	0.0125	0.00792	0.00857	0.00509	0.00593	0.00871	0.00938
4.2	0.01	0.0113	0.00681	0.00784	0.00445	0.0054	0.00741	0.00852
4.3	0.00895	0.0102	0.00642	0.00715	0.00452	0.00488	0.00689	0.00772
4.4	0.0091	0.0093	0.00688	0.00652	0.00527	0.00441	0.00731	0.00703
4.5	0.01	0.00842	0.0074	0.00593	0.00557	0.00399	0.00796	0.00637
4.6	0.0103	0.00764	0.0074	0.0054	0.00548	0.00363	0.00808	0.00579
4.7	0.0101	0.00691	0.00716	0.00491	0.00519	0.00328	0.00786	0.00524
4.8	0.00948	0.00623	0.00661	0.00443	0.00472	0.00297	0.0073	0.00473
4.9	0.00842	0.00564	0.00575	0.00402	0.00382	0.00267	0.00631	0.00428
5.0	0.00675	0.0051	0.00453	0.00365	0.0028	0.00242	0.00495	0.00388
5.1	0.00524	0.00465	0.00346	0.00331	0.0021	0.00219	0.00381	0.00353
5.2	0.00404	0.00426	0.00272	0.00302	0.0017	0.002	0.00298	0.00323
5.3	0.00329	0.00391	0.00224	0.00275	0.00143	0.0018	0.00245	0.00295
5.4	0.0028	0.00358	0.00189	0.0025	0.0012	0.00163	0.00208	0.0027
5.5	0.00239	0.00326	0.00159	0.00226	0.000999	0.00148	0.00176	0.00246
5.6	0.00202	0.00299	0.00136	0.00207	0.000841	0.00135	0.00149	0.00225
5.7	0.00175	0.00275	0.0012	0.00189	0.000777	0.00122	0.00131	0.00206
5.8	0.00163	0.0025	0.00113	0.00172	0.000788	0.00111	0.00125	0.00188
5.9	0.00161	0.0023	0.00113	0.00157	0.000798	0.001	0.00125	0.00172
6.0	0.00162	0.00212	0.00112	0.00142	0.000781	0.000916	0.00125	0.00158
6.1	0.00165	0.00198	0.0011	0.00132	0.000733	0.000833	0.00124	0.00147
6.2	0.00161	0.00187	0.00105	0.00123	0.000677	0.00076	0.0012	0.00138
6.3	0.00155	0.00178	0.000992	0.00114	0.000618	0.000699	0.00114	0.0013
6.4	0.00148	0.00168	0.000934	0.00107	0.000568	0.000638	0.00107	0.00122
6.5	0.00141	0.00159	0.000874	0.000998	0.000515	0.000583	0.00101	0.00115
6.6	0.00135	0.00152	0.00082	0.000931	0.000465	0.000534	0.000958	0.00108
6.7	0.00129	0.00146	0.000774	0.00087	0.000426	0.000491	0.000907	0.00103
6.8	0.00123	0.0014	0.000732	0.000821	0.000403	0.000449	0.000868	0.000979
6.9	0.00121	0.00135	0.000707	0.000772	0.000397	0.000412	0.000854	0.000936
7.0	0.00125	0.00131	0.00071	0.000723	0.000397	0.000381	0.000873	0.000902
7.1	0.00132	0.0013	0.00073	0.000699	0.000394	0.000351	0.000915	0.000882
7.2	0.0014	0.00129	0.00075	0.000681	0.000387	0.000327	0.000956	0.000865
7.3	0.00148	0.0013	0.000766	0.000662	0.000378	0.000302	0.000998	0.000862
7.4	0.00157	0.00132	0.000779	0.00065	0.000364	0.000284	0.00104	0.000868
7.5	0.00168	0.00136	0.000789	0.000644	0.000345	0.000266	0.00109	0.00088
7.6	0.00179	0.00143	0.000801	0.000644	0.000331	0.000253	0.00115	0.000916
7.7	0.00194	0.00156	0.000821	0.000662	0.000322	0.000247	0.00123	0.000983
7.8	0.00215	0.00176	0.000848	0.000699	0.000317	0.000253	0.00135	0.0011
7.9	0.00248	0.00214	0.000895	0.00076	0.000324	0.000278	0.00154	0.00133
8.0	0.00315	0.00287	0.000977	0.000876	0.000354	0.00032	0.00193	0.00175
8.1	0.00378	0.00348	0.00113	0.00103	0.000426	0.000388	0.00231	0.00213
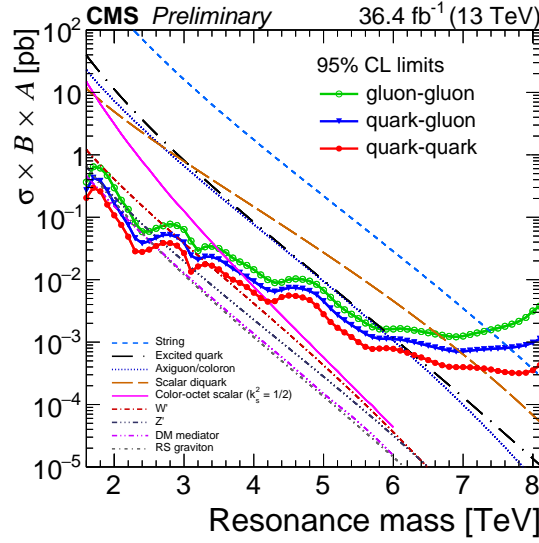
Figure 32: Summary of 95% CL asymptotic LHC CL$_s$ limits on $\sigma \times BR \times A$ for a gg resonance, a qg resonance, and a qq resonance.

Table 11: Observed and expected upper limits at 95% CL on $\sigma \times B \times A$ for a gg resonance, a qg resonance, and a qq resonance as a function of the resonance mass.

Mass [TeV]	95% CL upper limit [pb]					
	gg		qg		qq	
	Observed	Expected	Observed	Expected	Observed	Expected
500	2.892939e+01	3.525391e+01	3.563211e+01	3.837891e+01	4.301870e+01	4.472656e+01
550	4.057828e+01	3.134766e+01	3.288110e+01	2.685547e+01	1.754010e+01	1.333008e+01
600	3.868192e+01	2.080078e+01	2.889622e+01	1.879883e+01	1.334839e+01	1.030273e+01
650	1.415929e+01	1.762695e+01	9.830629e+00	1.137015e+01	4.682445e+00	5.102539e+00
700	6.703520e+00	1.118164e+01	4.134835e+00	6.225586e+00	2.463087e+00	3.112793e+00
750	5.725194e+00	8.081055e+00	4.051246e+00	4.675293e+00	2.546007e+00	2.388000e+00
800	9.982520e+00	7.104492e+00	5.685233e+00	4.138184e+00	3.099410e+00	2.130127e+00
850	1.122846e+01	5.834961e+00	5.272036e+00	3.308105e+00	2.026974e+00	1.777649e+00
900	6.429113e+00	4.113770e+00	3.132606e+00	2.374268e+00	1.171088e+00	1.369476e+00
950	2.827171e+00	3.283691e+00	1.439307e+00	1.715088e+00	5.949863e-01	1.077271e+00
1000	1.661260e+00	2.575684e+00	9.341059e-01	1.458740e+00	5.649927e-01	9.002686e-01
1050	1.393956e+00	2.191162e+00	1.095426e+00	1.251221e+00	8.651865e-01	7.843018e-01
1100	2.072613e+00	1.947021e+00	1.689552e+00	1.119995e+00	1.288036e+00	6.927490e-01
1150	3.899769e+00	1.763916e+00	2.058755e+00	1.034546e+00	1.391739e+00	6.378174e-01
1200	3.359706e+00	1.617432e+00	2.077571e+00	9.368896e-01	1.366382e+00	5.905151e-01
1250	3.443265e+00	1.446533e+00	2.039741e+00	8.575439e-01	1.222093e+00	5.340576e-01
1300	2.788742e+00	1.275635e+00	1.584951e+00	7.476807e-01	7.756045e-01	4.730225e-01
1350	1.983092e+00	1.107788e+00	9.166403e-01	6.439209e-01	4.547082e-01	4.180908e-01
1400	1.033955e+00	9.613037e-01	4.846376e-01	5.645752e-01	2.591259e-01	3.692627e-01
1450	6.086317e-01	8.331299e-01	3.429054e-01	4.852295e-01	1.999736e-01	3.204346e-01
1500	4.219341e-01	7.171631e-01	2.517672e-01	4.241943e-01	1.637878e-01	2.838135e-01
1550	3.245347e-01	6.256104e-01	1.906475e-01	3.753662e-01	1.386888e-01	2.471924e-01
1600	3.290328e-01	5.584717e-01	2.049665e-01	3.448486e-01	1.556278e-01	2.349854e-01

Figure 36 shows the local significance as a function of mass for a gg resonance, a qg resonance, and a qq resonance.

Figure 33: Local significance for a gg resonance (top left), a qg resonance (top right), and a qq resonance (bottom).

Figure 34: 95% CL asymptotic LHC CL$_s$ limits on $\sigma \times BR \times A$ for a gg resonance (top left), a qg resonance (top right), and a qq resonance (bottom left). Bottom right plot shows the gg and qq resonance limits weighted for the branching ratios of a Randall-Sundrum Graviton.

Figure 35: Summary of 95% CL asymptotic LHC CL$_\mathrm{s}$ limits on $\sigma \times BR \times A$ for a gg resonance, a qg resonance, and a qq resonance.
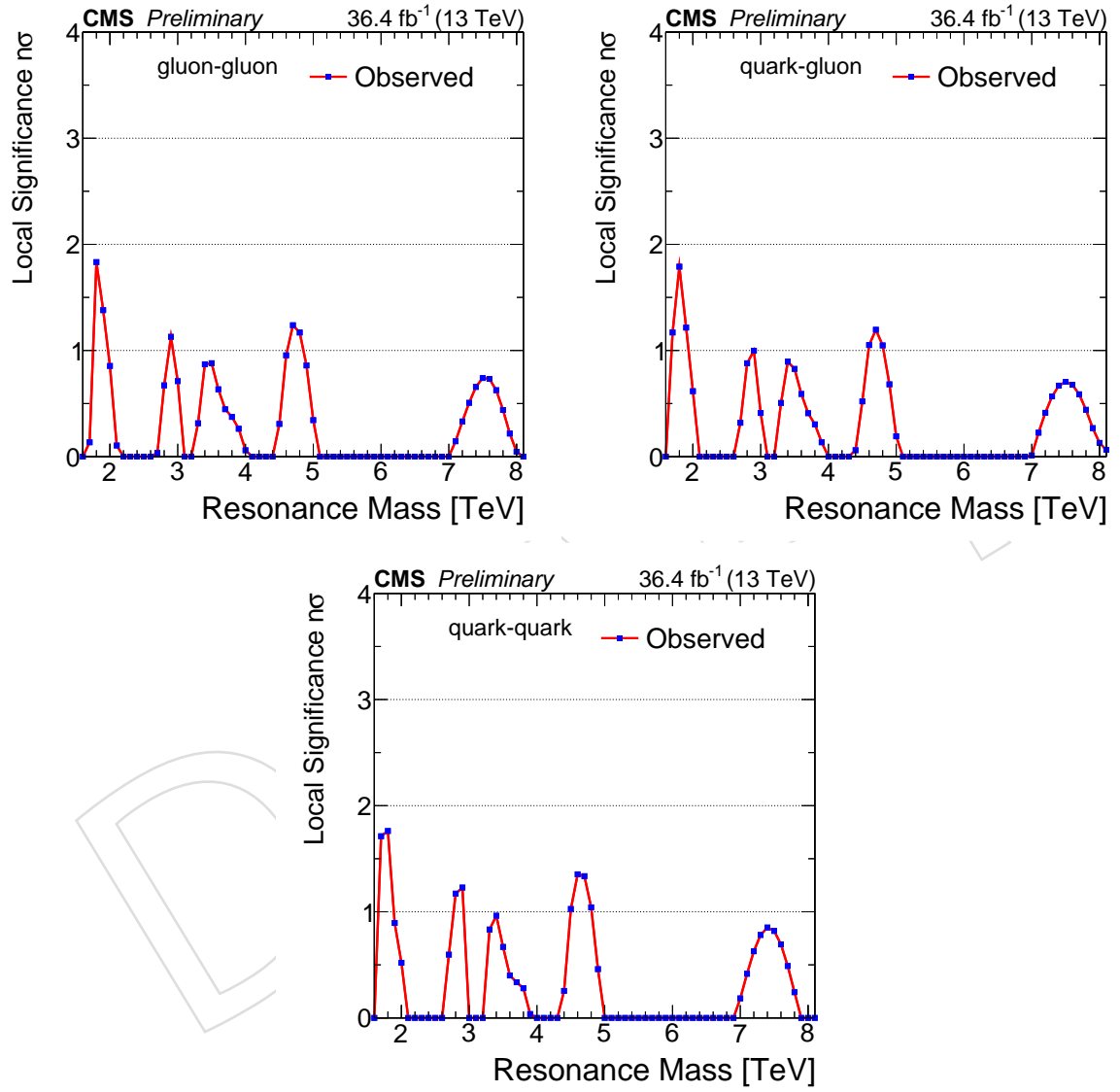
Figure 36: Local significance for a gg resonance (top left), a qg resonance (top right), and a qq resonance (bottom).
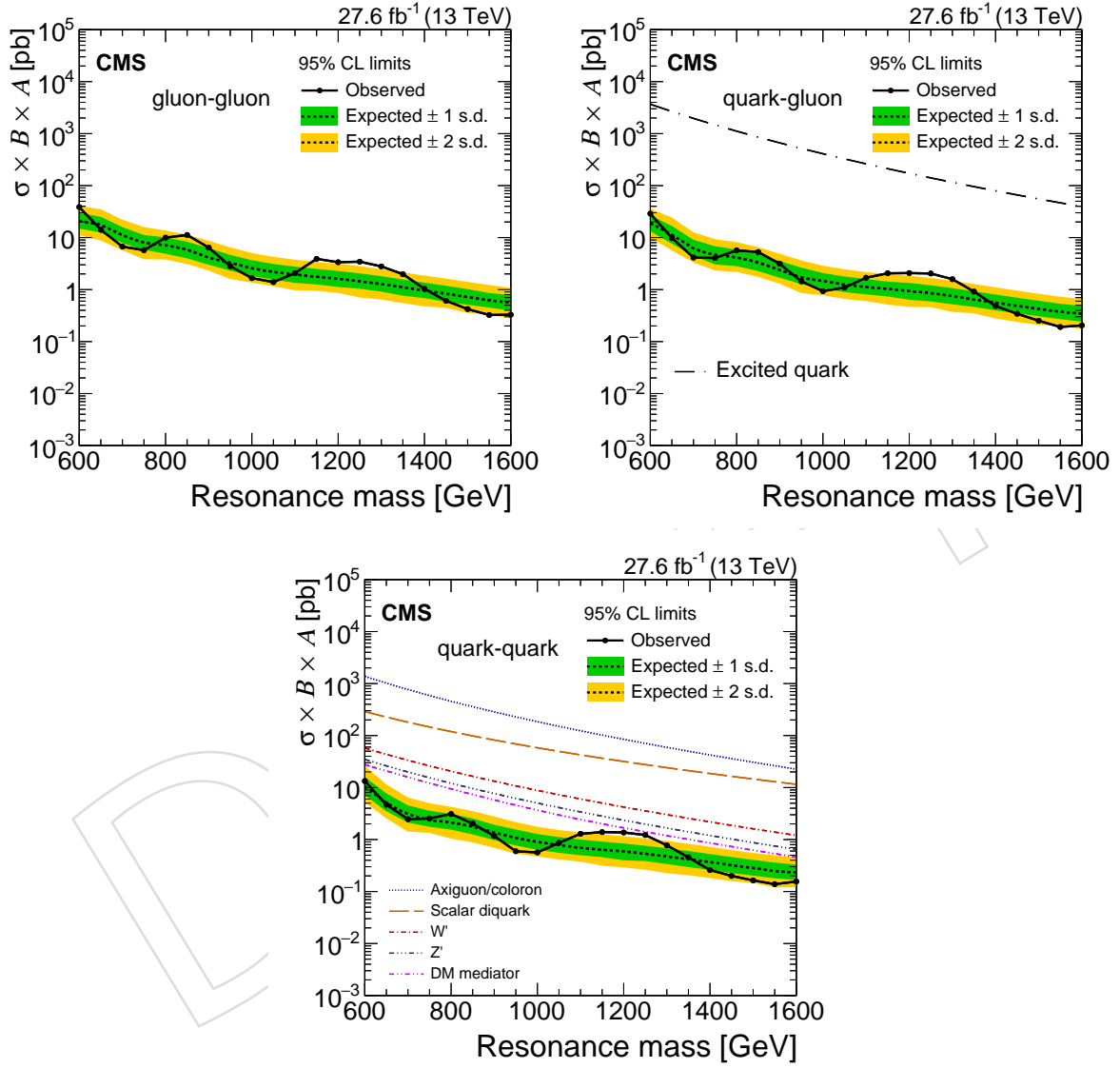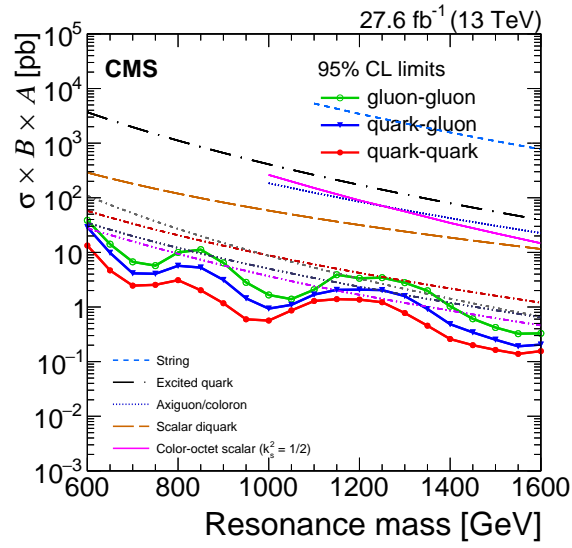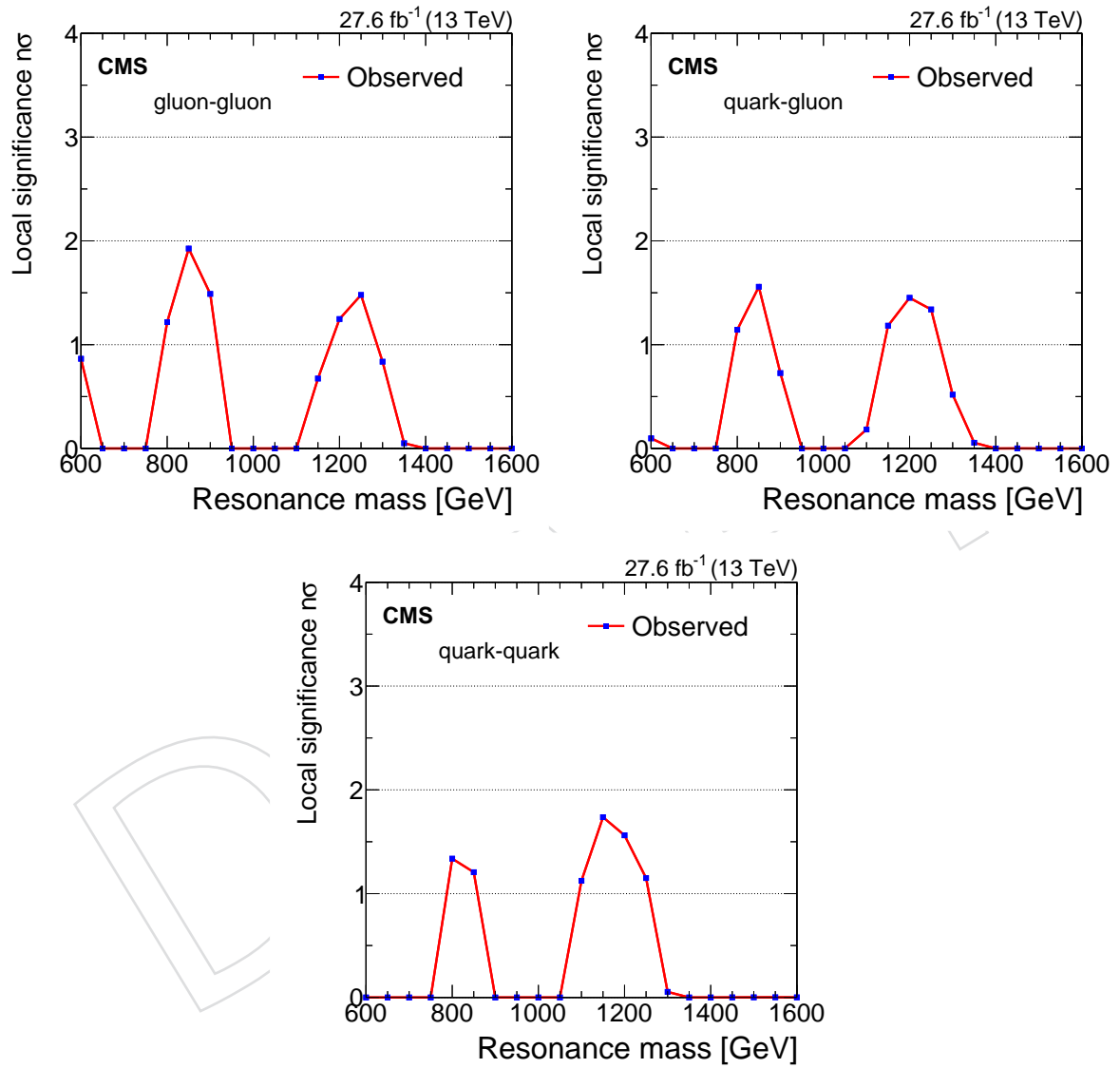
12   Mass Limits on Models of Dijet Resonances

Figure 31 (summarized in Fig. 32) and 34 show the model-independent observed upper limits at 95% confidence level (CL) on $\sigma B A$, i.e., the product of the cross section (σ), the branching fraction (B), and the acceptance (A) for the kinematic requirements $|\Delta\eta_{jj}| < 1.3$ and $|\eta| < 2.5$, for narrow resonances. The acceptance of the minimum dijet mass requirement in the analysis has been taken into account by correcting the limits, and therefore does not appear in the acceptance A. Figure 31 and 34 also show the expected limits on the cross section and their bands of uncertainty. The generated mass spectra are fit with a signal+background model to extract expected upper limits. The difference in the limits for qq and gg and Gaussian resonances at the same resonance mass originates from the difference in their lineshapes. We note that the limits from Gaussian resonances are smaller than can be expected from any physical model, as they do not have any tails due to radiation, and consequently they are narrower and located closer to the resonance pole than any combination of two partons can produce.

All upper limits presented can be compared to the parton-level predictions of $\sigma B A$, without detector simulation, to determine mass limits on new particles. The model predictions shown in Fig. 31 and 34 are calculated in the narrow-width approximation [1] using the CTEQ6L1 [27] PDF at leading order, with a next-to-leading order correction factor included for the W′, Z′, and axigluon/coloron models [28]. The acceptance is evaluated at the parton level for the resonance decay to two partons. In the case of isotropic decays it is $A \approx 0.6$ independent of resonance mass. For a given model, new particles are excluded at 95% CL in mass regions where the theoretical prediction lies at or above the observed upper limit for the appropriate final state of Fig. 34-31. For the RS graviton model, which couples to pairs of quarks or gluons with branching fractions reported in Appendix C, we obtain mass limits by comparing the RS graviton cross section curve to a weighted average of the limits in the quark-quark and gluon-gluon final states. The mass limits are reported in Table 12.

In Table 12, the mass limits on models of dijet resonances from the full 2016 analysis are also compared with those from the previous 2016 analysis using 12.9 fb^{-1}. The increase in the expected mass limits is roughly what is expected from the increased luminosity. The observed limits with the full 2016 data sample extend all of those obtained with the 12.9 fb^{-1} dataset. We also include the limits from the 13 TeV analysis with 2.4 fb^{-1} and from the 8 TeV analysis with 20 fb^{-1}.

Table 12: Observed and expected mass limits at 95% CL from this analysis with 36.4 fb^{-1} at $\sqrt{s} = 13$ TeV compared to previously published limits on narrow resonances from CMS with 12.9 fb^{-1} and 2.4 fb^{-1} at $\sqrt{s} = 13$ TeV [8, 9] and with 20 fb^{-1} at $\sqrt{s} = 8$ TeV [6]. The listed models are excluded between 0.6 TeV and the indicated mass limit by this analysis. *For the RS Graviton model, in addition to the observed mass limit listed below, this analysis also excludes the mass interval between 2.1 and 2.5 TeV.

| Model | Final State | Observed (expected) mass limit [TeV] | | | |
		36.4 fb^{-1} 13 TeV	12.9 fb^{-1} 13 TeV	2.4 fb^{-1} 13 TeV	20 fb^{-1} 8 TeV
String	qg	7.6 (7.7)	7.4 (7.4)	7.0 (6.9)	5.0 (4.9)
Scalar diquark	qq	7.2 (7.4)	6.9 (6.8)	6.0 (6.1)	4.7 (4.4)
Axigluon/coloron	q$\overline{q}$	6.2 (6.1)	5.5 (5.6)	5.1 (5.1)	3.7 (3.9)
Excited quark	qg	6.0 (5.8)	5.4 (5.4)	5.0 (4.8)	3.5 (3.7)
Color-octet scalar ($k_s^2 = 1/2$)	gg	3.5 (3.6)	3.0 (3.3)	—	—
W$'$	q$\overline{q}$	3.4 (3.6)	2.7 (3.1)	2.6 (2.3)	2.2 (2.2)
Z$'$	q$\overline{q}$	2.7 (3.0)	2.1 (2.3)	—	1.7 (1.8)
RS Graviton	q$\overline{q}$, gg	1.7* (2.2)	1.9 (1.8)	—	1.6 (1.3)
DM Mediator ($m_{\mathrm{DM}} = 1$ GeV)	q$\overline{q}$	2.6 (2.5)	2.0 (2.0)	—	—

13   Additional Dark Matter Interpretations

Dark matteris an unidentified type ofmatterdistinct from ordinary matter, dark energy andneutrinos. The name indicate that it does not interact or emit any electromagnetic radiation, which means its invisible to the entire EM spectrum. Although it has not been observed directly, abundant astrophysical evidence, such as gravitational lensing and its gravitational effect on visible matter, has revealed its existence. The standard model of cosmology indicates that 26.8 % of the universe are dark matter, 68.3% are dark energy and only 4.9% are ordinary matter, which means the majority of the universe is still remain unseen. These motivate us to search for dark matter, both in the space and in the LHC. However, since the interaction between dark matter and ordinary matter is uncertain, and there are plenty of models. We chose the simplified model [20] recommended by the LHC DM Working group to constraints on dark matter for LHC searches.

13.1   Model Considered

In the model we used, DM particle is assumed as a Dirac Fermion X and the particle mediating the interaction is exchanged in the s-channel.
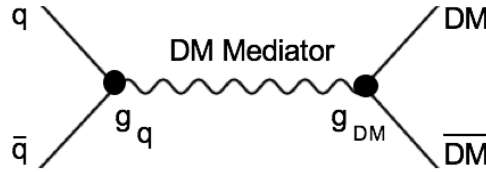

Figure 37: We only search for the process $q\bar{q} \rightarrow$ DM mediator$\rightarrow q\bar{q}$

After simplifying assumption [20], our model is characterized by four parameters: The DM mass m_{DM}, the mediator mass M_{med}, the universal mediator coupling to quarks gq and the mediator coupling to DM g_{DM}. The Two model with Spin-1 mediator Z', has the following Largrangins

$$\mathcal{L}_{vector} = -g_{DM}Z'_\mu\bar{\chi}\gamma^\mu\chi - g_q \sum_{q=u,d,s,c,b,t} Z'_\mu\bar{q}\gamma^\mu q \tag{12}$$

$$\mathcal{L}_{axial-vector} = -g_{DM}Z'_\mu\bar{\chi}\gamma^\mu\gamma_5\chi - g_q \sum_{q=u,d,s,c,b,t} Z'_\mu\bar{q}\gamma^\mu\gamma_5 q \tag{13}$$

The minimal decay width of the mediator is given by the sumof the partial widths for all decays into DM and quarks that are kinematically accessible. For Vector Mediator, the partial widths are given by

$$\Gamma^{\chi\bar{\chi}}_{\text{vector}} = \frac{g^2_{DM}M_{med}}{12\pi}(1-4z_{DM})^{1/2}(1+2z_{DM}) \tag{14}$$

$$\Gamma^{q\bar{q}}_{\text{vector}} = \frac{g^2_q M_{med}}{4\pi}(1-4z_q)^{1/2}(1+2z_q) \tag{15}$$

where $z_{DM,q} = m^2_{DM,q}/M^2_{med}$ and the two different types of contribution to the width vanish for $M_{med} < 2m_{DM,q}$. the corresponding expressions for the axial-vector mediator are

$$\Gamma^{\chi\bar{\chi}}_{\text{axial-vector}} = \frac{g^2_{DM}M_{med}}{12\pi}(1-4z_{DM})^{3/2} \tag{16}$$

$$\Gamma^{q\bar{q}}_{\text{axial-vector}} = \frac{g_q^2 M_{med}}{4\pi}(1 - 4z_q)^{3/2} \tag{17}$$

13.2 Result

In the simplified model which recommended by Ref [20], mediaters are only decay into qq and pairs of DM particles, with unknown mass m_{DM}. In this case, we set the universal quark coupling $g_q = 0.25$ and $g_{DM} = 1.0$. In order to find which energy of Dark matter and mediator is excluded, we do a scan over dark matter mass and mediator mass plane, using MGraph5. The lowest dark matter mass is 1GeV, indistinguishable from zero, and up to 1.4TeV, with 50GeV step. The lowest Mediator mass is 500GeV, up to 4TeV, with 0.5TeV step but 50 GeV step for the critical mass range, which is form 1800GeV to 2800GeV. In this simulation, we use the cross section of parton level to get for the exclusion range. The product of the cross section require a kinematic limit, which is $|\Delta\eta_{jj}| < 1.3$, $|\eta| < 2.5$ and the two jet mass (M_{jj}) within the 500GeV mass window of the resonances mass for narrow resonances. It should also be noted taht the excluded region strongly depends on the chosen couplings and the model scenario. In this situation, we will use the $m_{DM} = 1GeV$ for the scan.

Figure 38: The 95% CL uppper limits on the product of the cross section, branching fraction, and acceptance for quark-quark type dijet resonances, compared with predicted cross sections of dark matter mediators for $m_{DM} = 0.3, 1, 1.4TeV$, for both Vector and Axial-Vector model.

Figure 38 show cross section of 3 citical dark matter mass with all mediator mass, for both types of mediator. All the observed point below the upper limit line are excluded from this search. The mediator cross section increases with increasing DM mass. Actually, the curve dip where the mediator starts to decay into DM, which will reduce the cross section. Furthermore, the dip is more pronounced for the vector model where the Dm decay channel become faster as a function of increasing mediator mass. For each dark matter mass, we would use the cross section of each Mediator mass to compare with the observed 95% CL upper limit for quark-quark to find the exclusion Mediator mass of the individual dark matter mass. After all dark matter mass is compared, we will have a 2D exclusion area on the dark matter mass vs. mediator mass, for axial-vector mediator and vector mediator.

Figure 39 shows the the excluded values of mediator mass as a function of m_{DM} for both types of mediators. For $m_{DM} = 1GeV$, indistinguishable from zero, the exclusion range of Mediator mass (M_{Med}) is around 0.6 to 2.6 TeV. if $m_{DM} > M_{Med}/2$, the mediator cannot decay to DM particles, and the dijet cross section from the mediator models becomes identical to that in the leptophbic-phobic Z' model used in Figure 40 with a coupling $g'_q = g_q = 0.25$. Therefore for these values of mDM the limits on the mediator mass in figure 39 are identical to the limits on the Z' mass at g'_q=0.25 in figure 40. Similarly, if $m_{DM} = 0$, the limits on the mediator mass in figure 39 are identical to the limits on the Z' mass at $g'_q = g_q/\sqrt{1 + 16/(3N_f)} \approx 0.182$ in figure 40 , where N_f is the effective number of quark flavors contributing to the width of the resonance. As outlined in detail in Ref. [20] these results can also be compared with results from direct detection experiments. The limits in figure 39 are first re-calculated at 90% CL, and then translated into the plane of the DM mass versus the DM-nucleon interaction cross section from the pre- dicted relation between the interaction cross section and the mediator mass. An axial-vector mediator leads to a spin-dependent cross section, σ^{SD}, and a vector mediator leads to a spin independent cross section, σ^{SI}. For our benchmark model the present search excludes a significantly smaller σ^{SD} than the direct detection experiments, and a competitive region of
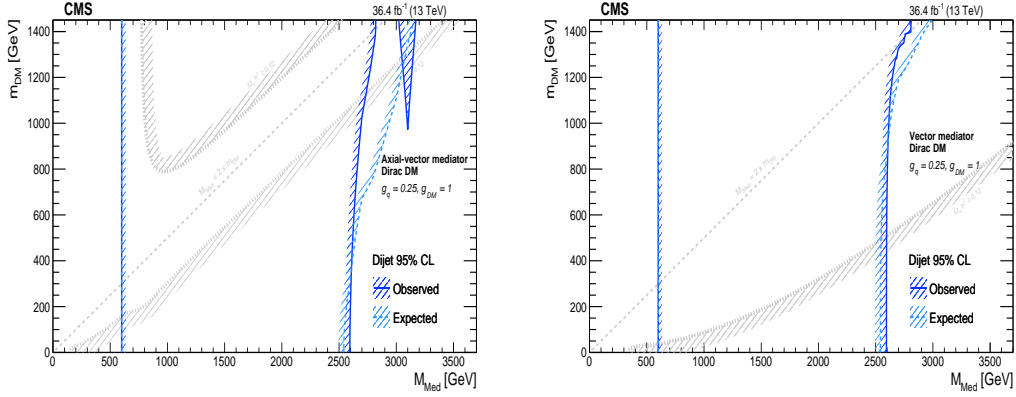
Figure 39: The 95% CL observed (solid) and expected (dashed) excluded regions in the plane of dark matter mass vs. mediator mass, for an axial-vector mediator(left) and a vector mediator (right), are compared to contraints from the cosmological relic density of DM(light gray) determined rom astrophysical measurement and $M_{AD}DM$ version 2.0.6 as described in Ref [29]

.

σ^{SI}. We note that the absolute exclusion of this search, as well as its relative importance with respect to other dark matter searches, strongly depends on the chosen coupling and model scenario. Nevertheless,this benchmark model, a vector or an axial-vector mediator with a universal quark coupling $g_q = 0.25$ and a DM coupling of $g_{DM} = 1.0$, illustrates that dijet searches can place significant bounds on relevant DM models and thus are important ingredients in the search for DM.
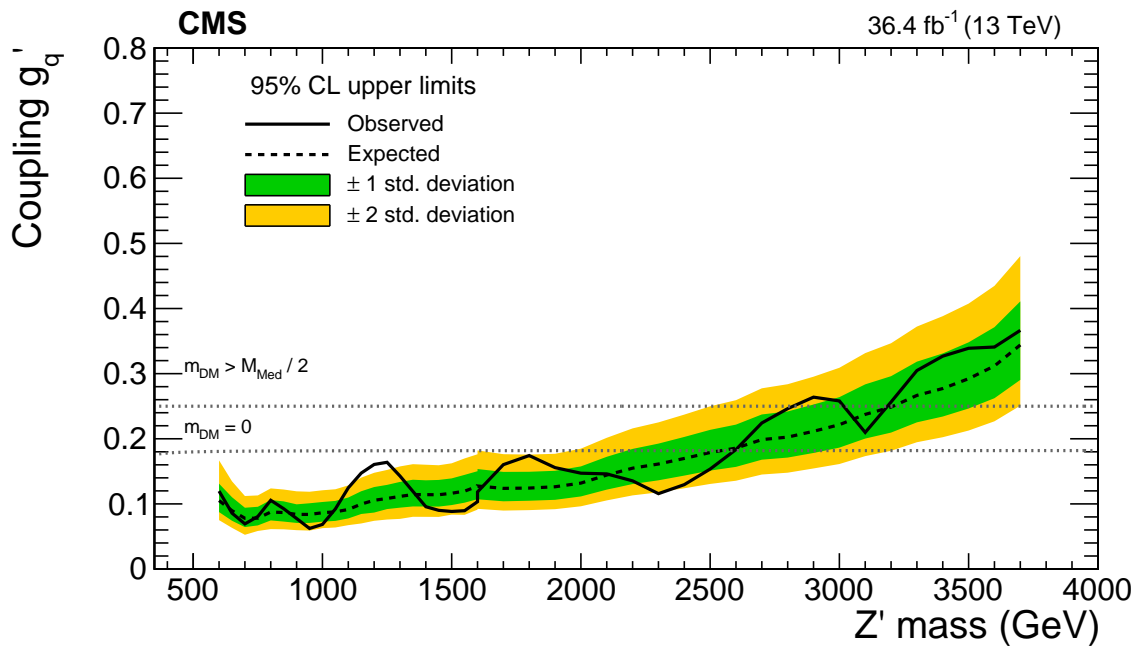
Figure 40: The 95% Cl upperlimits on the universal quark coupling g'_q as a function of resonance mass for a leptonphobic Z' resonance that only couples to quarks. This show the observed limits (solid), expected limits (dashed) and their variation at the 1 and 2 standard deviation levels (shaded bands). Dotted horizontal lines are also shown as the coupling strength for which the cross section for dijet production in this model is the same as for a DM mediator. AS WE GO TO PRESS THERE IS A KNOWN PROBLEM IN THE EXPECTED LIMIT BAND WHICH IS TOO LARGE FOR MASSES GREATER THAN 1600 GEV

14   Conclusions

In summary, two searches for narrow resonances decaying into a pair of jets have been performed using pp collisions at $\sqrt{s} = 13\,\text{TeV}$ corresponding to an integrated luminosity of $36.4\,\text{fb}^{-1}$. A low mass search using data scouting from the HLT trigger with calorimeter jets and a high mass search using particle flow jets. The dijet mass spectra have been measured to be smoothly falling distributions. In the analyzed data samples, there is no evidence for resonant particle production. We present generic upper limits on the product $\sigma B A$ that are applicable to any model of narrow dijet resonance production. We set mass limits at 95% CL on models of string resonances, scalar diquarks, excited quarks, axigluons, colorons, color octet scalars, W' bosons, Z' bosons, dark matter mediators, and RS Gravitons, which extend previously published limits in the dijet channel.

A Dijet mass binning

This is the dijet mass binning used in this analysis and all previous dijet resonance searches and also the 8 TeV dijet SMP measurements during run 1.

```
const int nMassBins = 103;

double massBoundaries[nMassBins+1] = {1, 3, 6, 10, 16, 23, 31, 40, 50, 61, 74, 88, 103,
119, 137, 156, 176, 197, 220, 244, 270, 296, 325, 354, 386, 419, 453, 489, 526, 565, 606,
649, 693, 740, 788, 838, 890, 944, 1000, 1058, 1118, 1181, 1246, 1313, 1383, 1455, 1530,
1607, 1687, 1770, 1856, 1945, 2037, 2132, 2231, 2332, 2438, 2546, 2659, 2775, 2895, 3019,
3147, 3279, 3416, 3558, 3704, 3854, 4010, 4171, 4337, 4509, 4686, 4869, 5058, 5253, 5455,
5663, 5877, 6099, 6328, 6564, 6808, 7060, 7320, 7589, 7866, 8152, 8447, 8752, 9067, 9391,
9726, 10072, 10430, 10798, 11179, 11571, 11977, 12395, 12827, 13272, 13732, 14000};
```

B   Comparison with earlier results

For comparing the stability of CMS dijet results the ratio of the full 2016 dijet spectrum and the published 2015 result is shown left and the ratio of full 2016 data with ICHEP 2016 data is shown right in Fig. 41. The older datasets are in numerator.

The full 2016 dataset is in good agreement with the 2015 result and no significant slope is observed, although there is a constant shift of 7% which could be due to minuscule difference in jet energy scale or due to differences in luminosity calculations. When comparing the 2016 ICHEP result to the full 2016 result we observe a steady slope showing that the 2016 ICHEP spectrum is higher at high dijet mass. This is however understood to be a result of the jet energy scale corrections used for the ICHEP result (Spring16_V6) which are now understood to have corrected high energy jets too much. The conditions for 2015 results are much better understood than ICHEP 2016 conditions, so we are not worried about the difference of full 2016 and 2016 ICHEP results. The differences between the datasets are all within the jet energy scale uncertainties.
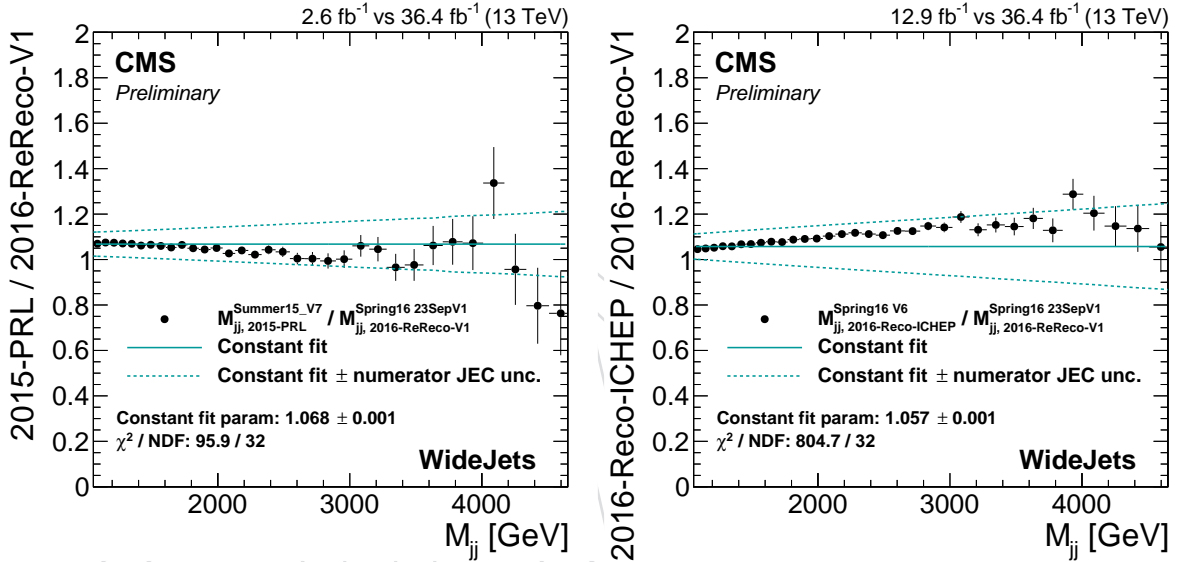

Figure 41: On the left we compare the published 2015 dijet mass spectrum and on the right the 2016 ICHEP spectrum to the full 2016 spectrum.

C Randall-Sundrum branching fractions

Table 13: Total cross section and braching fraction of a Randall-Sundrum Graviton as a function of the resonance mass.

Mass [GeV]	Total xsec [pb]	Branching fractions			
		$gg \to qq$	$gg \to gg$	$qq \to qq$	$qq \to gg$
1600.0	0.6666E+00	0.40300	0.18393	0.17385	0.23922
1700.0	0.4691E+00	0.38497	0.17570	0.18490	0.25442
1800.0	0.3349E+00	0.36746	0.16771	0.19564	0.26919
1900.0	0.2424E+00	0.35061	0.16002	0.20596	0.28340
2000.0	0.1774E+00	0.33436	0.15260	0.21592	0.29711
2100.0	0.1312E+00	0.31881	0.14551	0.22545	0.31022
2200.0	0.9793E-01	0.30389	0.13870	0.23460	0.32281
2300.0	0.7373E-01	0.28971	0.13223	0.24329	0.33477
2400.0	0.5591E-01	0.27615	0.12604	0.25160	0.34620
2500.0	0.4269E-01	0.26330	0.12017	0.25948	0.35705
2600.0	0.3279E-01	0.25106	0.11459	0.26698	0.36737
2700.0	0.2533E-01	0.23947	0.10929	0.27409	0.37715
2800.0	0.1966E-01	0.22848	0.10428	0.28083	0.38642
2900.0	0.1532E-01	0.21804	0.09951	0.28723	0.39522
3000.0	0.1200E-01	0.20818	0.09501	0.29327	0.40354
3100.0	0.9422E-02	0.19880	0.09074	0.29902	0.41145
3200.0	0.7426E-02	0.18996	0.08670	0.30444	0.41891
3300.0	0.5870E-02	0.18157	0.08287	0.30958	0.42598
3400.0	0.4652E-02	0.17363	0.07924	0.31445	0.43268
3500.0	0.3696E-02	0.16613	0.07582	0.31905	0.43901
3600.0	0.2942E-02	0.15900	0.07257	0.32341	0.44502
3700.0	0.2346E-02	0.15226	0.06949	0.32755	0.45070
3800.0	0.1874E-02	0.14587	0.06658	0.33146	0.45609
3900.0	0.1499E-02	0.13982	0.06381	0.33517	0.46120
4000.0	0.1200E-02	0.13408	0.06120	0.33869	0.46603
4100.0	0.9625E-03	0.12865	0.05872	0.34202	0.47062
4200.0	0.7724E-03	0.12349	0.05636	0.34518	0.47497
4300.0	0.6202E-03	0.11860	0.05413	0.34818	0.47909
4400.0	0.4983E-03	0.11396	0.05201	0.35102	0.48301
4500.0	0.4005E-03	0.10956	0.05001	0.35372	0.48671
4600.0	0.3220E-03	0.10539	0.04810	0.35627	0.49023
4700.0	0.2589E-03	0.10142	0.04629	0.35871	0.49358
4800.0	0.2082E-03	0.09766	0.04457	0.36101	0.49675
4900.0	0.1673E-03	0.09409	0.04295	0.36320	0.49976
5000.0	0.1345E-03	0.09070	0.04140	0.36528	0.50262
5100.0	0.1080E-03	0.08748	0.03993	0.36725	0.50534
5200.0	0.8669E-04	0.08444	0.03854	0.36912	0.50791
5300.0	0.6953E-04	0.08153	0.03721	0.37090	0.51036
5400.0	0.5573E-04	0.07879	0.03596	0.37258	0.51267
5500.0	0.4462E-04	0.07619	0.03478	0.37417	0.51486
5600.0	0.3568E-04	0.07372	0.03364	0.37569	0.51695
5700.0	0.2850E-04	0.07138	0.03258	0.37712	0.51892
5800.0	0.2273E-04	0.06917	0.03157	0.37848	0.52079
5900.0	0.1810E-04	0.06707	0.03061	0.37976	0.52256
6000.0	0.1439E-04	0.06509	0.02971	0.38098	0.52422
6100.0	0.1142E-04	0.06321	0.02885	0.38213	0.52581
6200.0	0.9042E-05	0.06145	0.02805	0.38321	0.52730
6300.0	0.7147E-05	0.05978	0.02729	0.38423	0.52870
6400.0	0.5635E-05	0.05821	0.02657	0.38520	0.53003
6500.0	0.4433E-05	0.05673	0.02589	0.38610	0.53127
6600.0	0.3479E-05	0.05534	0.02526	0.38695	0.53245
6700.0	0.2722E-05	0.05404	0.02466	0.38775	0.53355
6800.0	0.2125E-05	0.05282	0.02411	0.38850	0.53458
6900.0	0.1653E-05	0.05167	0.02358	0.38920	0.53554
7000.0	0.1282E-05	0.05060	0.02309	0.38986	0.53645
7100.0	0.9914E-06	0.04961	0.02264	0.39047	0.53728
7200.0	0.7639E-06	0.04867	0.02221	0.39104	0.53807
7300.0	0.5866E-06	0.04780	0.02182	0.39157	0.53881
7400.0	0.4489E-06	0.04700	0.02145	0.39206	0.53948
7500.0	0.3423E-06	0.04625	0.02111	0.39252	0.54011
7600.0	0.2599E-06	0.04555	0.02079	0.39296	0.54071
7700.0	0.1966E-06	0.04489	0.02049	0.39336	0.54126
7800.0	0.1481E-06	0.04428	0.02021	0.39373	0.54178
7900.0	0.1112E-06	0.04370	0.01994	0.39409	0.54227
8000.0	0.8308E-07	0.04314	0.01969	0.39443	0.54274
8100.0	0.6183E-07	0.04260	0.01944	0.39476	0.54319

References

[1] R. M. Harris and K. Kousouris, "Searches for dijet resonances at hadron colliders",
International Journal of
Modern Physics A **26** (2011), no. 30n31, 5005–5055, `doi:10.1142/S0217751X11054905`,
`arXiv:http://www.worldscientific.com/doi/pdf/10.1142/S0217751X11054905`.

[2] CMS Collaboration, "Search for Dijet Resonances in 7 TeV pp Collisions at CMS", *Phys.*
Rev. Lett. **105** (2010) 211801, `doi:10.1103/PhysRevLett.105.211801`,
`arXiv:1010.0203`. [Publisher's note: `doi:10.1103/PhysRevLett.106.029902`].

[3] CMS Collaboration, "Search for resonances in the dijet mass spectrum from 7 TeV pp
collisions at CMS", *Phys. Lett. B* **704** (2011) 123,
`doi:10.1016/j.physletb.2011.09.015`, `arXiv:1107.4771`.

[4] CMS Collaboration, "Search for narrow resonances and quantum black holes in inclusive
and b-tagged dijet mass spectra from pp collisions at $\sqrt{s} = 7$ TeV", *JHEP* **01** (2013) 013,
`doi:10.1007/JHEP01(2013)013`, `arXiv:1210.2387`.

[5] CMS Collaboration, "Search for narrow resonances using the dijet mass spectrum in pp
collisions at $\sqrt{s} = 8$ TeV", *Phys. Rev. D* **87** (2013) 114015,
`doi:10.1103/PhysRevD.87.114015`, `arXiv:1302.4794`.

[6] CMS Collaboration, "Search for resonances and quantum black holes using dijet mass
spectra in proton-proton collisions at $\sqrt{s} = 8$ TeV", *Phys.Rev.* **D91** (2015), no. 5, 052009,
`doi:10.1103/PhysRevD.91.052009`, `arXiv:1501.04198`.

[7] CMS Collaboration, "Search for narrow resonances in dijet final states at sqrt(s)=8 TeV
with the novel CMS technique of data scouting", `arXiv:1604.08907`.

[8] CMS Collaboration, "Search for narrow resonances decaying to dijets in proton-proton
collisions at $\sqrt{(s)} = 13$ TeV", *Phys. Rev. Lett.* **116** (2016), no. 7, 071801,
`doi:10.1103/PhysRevLett.116.071801`, `arXiv:1512.01224`.

[9] CMS Collaboration, "Search for dijet resonances in proton-proton collisions at $\sqrt{s} = 13$
TeV and constraints on dark matter and other models", *Submitted to: Phys. Lett. B* (2016)
`arXiv:1611.03568`.

[10] L. A. Anchordoqui et al., "Dijet Signals for Low Mass Strings at the LHC", *Phys. Rev. Lett.*
101 (2008) 241803, `doi:10.1103/PhysRevLett.101.241803`, `arXiv:0808.0497`.

[11] S. Cullen, M. Perelstein, and M. E. Peskin, "TeV strings and collider probes of large extra
dimensions", *Phys. Rev. D* **62** (2000) 055012, `doi:10.1103/PhysRevD.62.055012`,
`arXiv:hep-ph/0001166`.

[12] CMS Collaboration, "Search for Dijet Resonances in the Dijet Mass Spectrum in pp
Collisions at $\sqrt{s} = 7$ TeV", *CMS AN* **2011/203** (2011).

[13] U. Baur, I. Hinchliffe, and D. Zeppenfeld, "EXCITED QUARK PRODUCTION AT
HADRON COLLIDERS", *Int. J. Mod. Phys.* **A2** (1987) 1285.

[14] J. Bagger, C. Schmidt, and S. King, "Axigluon production in hadronic collisions", *Phys.*
Rev. D **37** (1988) 1188, `doi:10.1103/PhysRevD.37.1188`.

[15] R. S. Chivukula, A. G. Cohen, and E. H. Simmons, "New Strong Interactons at the Tevatron ?", *Phys. Lett.* **B380** (1996) 92–98, `arXiv:hep-ph/9603311`.

[16] J. L. Hewett and T. G. Rizzo, "LOW-ENERGY PHENOMENOLOGY OF SUPERSTRING INSPIRED E(6) MODELS", *Phys. Rept.* **183** (1989) 193.

[17] T. Han, I. Lewis, and Z. Liu, "Colored resonant signals at the lhc: largest rate and simplest topology", *JHEP* **12** (2010) 085, `doi:10.1007/JHEP12(2010)085`, `arXiv:1010.4309`.

[18] R. Sekhar Chivukula, E. H. Simmons, and N. Vignaroli, "Distinguishing dijet resonances at the LHC", *Phys. Rev.* **D91** (2015), no. 5, 055019, `doi:10.1103/PhysRevD.91.055019`, `arXiv:1412.3094`.

[19] E. Eichten, I. Hinchliffe, K. D. Lane, and C. Quigg, "SUPER COLLIDER PHYSICS", *Rev. Mod. Phys.* **56** (1984) 579–707.

[20] A. Boveia et al., "Recommendations on presenting LHC searches for missing transverse energy signals using simplified s-channel models of dark matter", (2016). `arXiv:1603.04156`.

[21] J. Abdallah et al., "Simplified models for dark matter searches at the LHC", *Phys. Dark Univ.* **9-10** (2015) 8, `doi:10.1016/j.dark.2015.08.001`, `arXiv:1506.03116`.

[22] L. Randall and R. Sundrum, "Large Mass Hierarchy from a Small Extra Dimension", *Phys. Rev. Lett.* **83** (1999) 3370, `doi:10.1103/PhysRevLett.83.3370`, `arXiv:hep-ph/9905221`.

[23] CMS Collaboration, "Search for narrow resonances decaying to dijets in proton-proton collisions at $\sqrt{(s)} = 13$ TeV", *Phys. Rev. Lett.* **116** (2016), no. 7, 071801, `doi:10.1103/PhysRevLett.116.071801`, `arXiv:1512.01224`.

[24] CMS Collaboration, "Search for resonances and quantum black holes using dijet mass spectra in proton-proton collisions at $\sqrt{s} = 8$ TeV", *Phys. Rev.* **D91** (2015), no. 5, 052009, `doi:10.1103/PhysRevD.91.052009`, `arXiv:1501.04198`.

[25] The 13 TeV Dijet Team, "Search for narrow resonances using the dijet mass spectrum in proton-proton collisions at $\sqrt{s} = 13$ TeV (Phys14 MC analysis)", *CMS AN* **2015/063** (2015).

[26] The 13 TeV Dijet Team, "Search for narrow resonances decaying to dijets in pp collisions at $\sqrt{s} = 13$ TeV using 12.9 fb^{-1}", *CMS AN* **2016/202** (2016).

[27] J. Pumplin et al., "New generation of parton distributions with uncertainties from global QCD analysis", *JHEP* **07** (2002) 012, `doi:10.1088/1126-6708/2002/07/012`, `arXiv:hep-ph/0201195`.

[28] R. S. Chivukula, E. H. Simmons, A. Farzinnia, and J. Ren, "Hadron collider production of massive color-octet vector bosons at next-to-leading order", *Phys. Rev. D* **87** (2013) 094011, `doi:10.1103/PhysRevD.87.094011`, `arXiv:1303.1120`.

[29] T. du Pree, K. Hahn, P. Harris, and C. Roskas, "Cosmological constraints on Dark Matter models for collider searches", `arXiv:1603.04156`.